7.2 ION IRRADIATION CHARACTERIZATION STUDIES OF MAX PHASE CERAMICS – D.W. Clark[1], S.J. Zinkle[1,2], M.K. Patel[1], C.M. Parish[2] ([1]University of Tennessee, Knoxville, [2]Oak Ridge National Laboratory)

OBJECTIVE

This report presents results of research aimed to characterize the radiation resistance of three leading-candidate MAX Phase materials using ion beam irradiation techniques.

SUMMARY

Ti_3AlC_2, Ti_2AlC and Ti_3SiC_2 MAX phase ceramics were irradiated with 5.8 MeV Ni ions to midrange doses of 10 and 30 dpa at 400 and 700°C. In all cases, the materials remain fully crystalline. X-ray diffraction and nanoindentation show anisotropic swelling and hardening in all materials, with Ti_3AlC_2 and Ti_2AlC exhibiting more pronounced property changes than Ti_3SiC_2. In all three materials there is little damage dependence on dose (suggesting saturation of radiation damage at levels below 10 dpa) and significantly less retained damage at higher temperatures. SEM surface analysis showed significant grain boundary cracking in the aluminum based MAX phase irradiated at 400°C. Ti_3AlC_2 and Ti_2AlC do not appear to be suitable for irradiation applications near 400°C whereas the Ti_3SiC_2 is overall more damage tolerant.

PROGRESS AND STATUS

Introduction

A promising but as yet unproven class of material known as MAX Phase Ceramics (or simply MAX Phases) represents a relatively new class of solids best described as *thermodynamically stable nanolaminates*. MAX Phases are a family of layered compounds with chemical formula $M_{n+1}AX_n$, where M is an early transition metal, A is an element from the IIIA or IVA groups, X is carbon or nitrogen, and *n* = *1, 2*, or *3* [1-5]. The atomic stacking is based on a layered hexagonal close packed (HCP) crystal structure with alternating layers of close-packed M-atoms and X-atoms filling octahedral sites (comprising a formula identical to those found in the rock salt structure of MX binaries), and layers of pure A-group elements. Due to their unique crystal structure, MAX phases combine many attractive properties of both ceramics and metals. These properties include high temperature stability, high stiffness, good electrical and thermal conductivity, fracture toughness, thermal shock resistance, and machinability [1-5]. Certain MAX phases also promise good oxidation resistance and chemical compatibility [6]. While most of these materials physical properties have been documented, studies exploring the radiation properties the MAX phases have only recently begun.

Although radiation response mechanisms of the MAX phase ceramics are still relatively unexplored, some preliminary knowledge can be drawn from low dose, low temperature irradiation experiments that have been completed to date. The first and most basic conclusion is that the MAX phases are expected to follow physical and mechanical property change trends similar to those seen in traditional HCP ceramics. Secondly, previous experiments suggest that the MAX phases are generally resistant to amorphization up to relatively high doses (~25 dpa) following irradiation between 25˚C and 500˚C. This has been confirmed using selected area electron diffraction (SAED) and transmission electron microscopy (TEM) imaging techniques in Ti_3SiC_2 and Ti_3AlC_2 at ~25 dpa [4], and using SAED, TEM, x-ray diffraction (XRD), and nanoindentation for Ti_3SiC_2 at lower damage levels (~5 dpa) for multiple irradiation conditions between RT and 500˚C. Based on these studies, amorphization is not expected to be an issue at relevant fusion reactor temperatures of ~300-1000 C [1, 7-14]. Additionally, there is no evidence of void formation in Ti_3SiC_2 and Ti_3AlC_2 up to 500˚C and ~25 dpa [12], suggesting that vacancies are immobile below 500˚C (or else void nucleation and growth is strongly suppressed). These two factors hint that 25˚C and 500˚C in MAX phases correspond to temperatures above recovery Stage I (onset for interstitial motion) and below recovery Stage III (onset for vacancy motion), respectively [15, 16]. Finally, X-ray diffraction, TEM and nanoindentation results suggest that the MAX phases have a positive correlation between temperature and radiation damage recovery. This is manifest in the decrease in crystalline lattice disorder and defects observed at higher irradiation temperature conditions by XRD and TEM [7, 9-

11, 17], as well as a pronounced decrease in nanoindentation hardness at higher irradiation temperatures [8, 14], again suggesting mobile interstitials and immobile vacancies ("point defect swelling" regime). Hence, it is hypothesized that the MAX phases may have substantial radiation resistance up to relatively high damage levels between 25 and 500˚C or higher.

Experimental Procedure

The MAX phase bulk samples used in this experiment were synthesized and provided by Darin Tallman at Drexel University; a detailed explanation of the synthesis and processing conditions is discussed elsewhere [18, 19]. The bulk samples were subsequently sectioned, cut into ~3 mm diameter disks, ground to ~0.6 mm, and polished using diamond lapping film and colloidal silica suspension on polishing cloth. After the final polishing, the 3 mm diameter disk samples had a nominal final thickness of 0.55 mm. The samples were irradiated to midrange doses of 10 and 30 displacements per atom, at temperatures of 400 and 700˚C, at the Texas A&M Accelerator Laboratory using 5.8 MeV Ni^{++} ions. The correlation between ion fluence and displacements per atom was determined using SRIM 2013, recommendations from Stoller [20], and an assumed atomic displacement energy of 30 eV. A graphic of normalized displacements per atom (dpa) versus ion penetration depth for all three materials can be seen in Figure 1, with the selected area for post-irradiation analysis defined by the red box. A list of irradiation conditions and corresponding fluences for the four batches can be seen in Table 1.

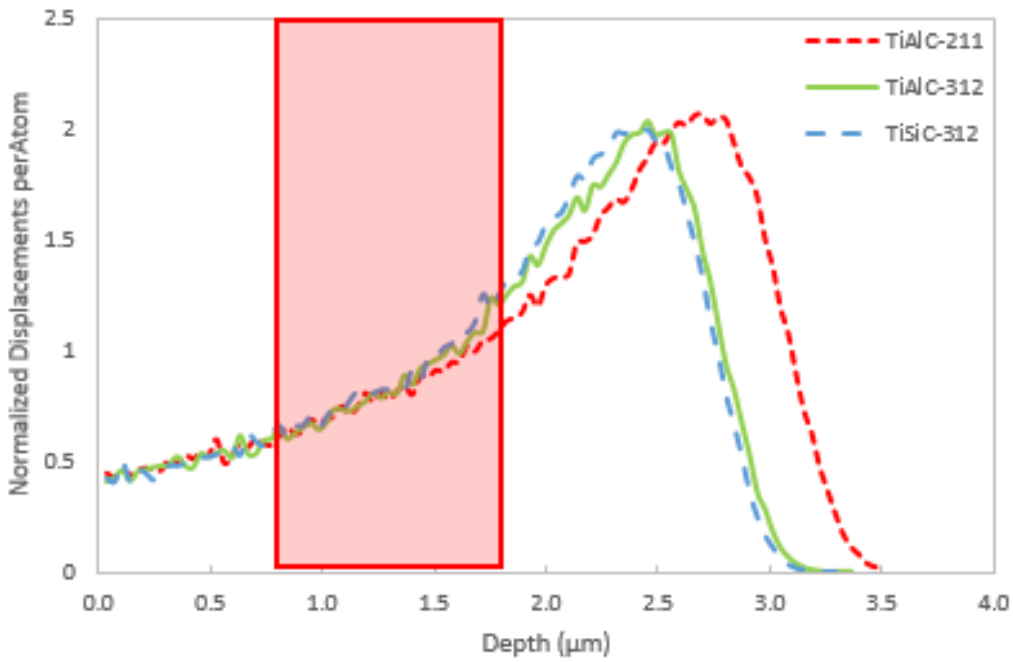

Figure 1. Normalized damage versus depth profiles for 5.8 MeV Ni^{4+} ions MAX phase ceramics.

Table 1 List of irradiation conditions and corresponding fluences.

Midrange Dose (dpa)	Fluence (ion/cm^2)	Temp. (°C)
10	2.43E+16	400
10	2.43E+16	700
30	7.30E+16	400
30	7.30E+16	700

Following irradiation, small scale analysis techniques were used to analyze the ~1.5-3 μm deep, thin film irradiated region. These techniques included grazing incidence X-ray diffraction, nanoindentation, scanning electron microscopy (SEM) and TEM.

To determine lattice parameter swelling, a GXRD capable X'Pert/PANalytical XRD machine was used to analyze the irradiated MAX phase samples. Due to the small irradiated sample size and aperture constraints, samples were mounted on single crystal silicon to provide a nearly zero background plate test environment. The incident beam angle, ω, was calculated using the computer program HighScore Plus to achieve an approximate maximum beam depth of 1.5 μm, which corresponds to the depth for the nominal midrange dose. In order to analyze diffraction patterns, the computer programs CMPR and Highscore Plus were used to find peak positions and match ICSD crystal patterns respectively [21, 22].

An Agilent nanoindenter with a Berkovich diamond indenter tip was used to examine the change of hardness and elastic modulus of the irradiated surface region. The indents were completed using a constant load rate of 500 μN/s (continuous stiffness mode) and preformed up to a depth 1100 nm. Optimized indentation positions were manually chosen using an optical microscope attached to the instrument. The areas considered optimized were those that appeared to be optically pristine and devoid of flaws, including scratches, pull-out, secondary phases, contamination, etc. To avoid the effect of strain fields, the distance between indents, large scratches, and sample edges was at least 50 μm. Approximately twenty indents were made per sample to obtain a good statistical average. Hardness and elastic modulus were then determined as functions of indentation depth using the software associated with indenter [23]. When analyzing the nanoindentation data, it was crucial to determine the transition point between the irradiated and substrate regions. This transition depth was determined by plotting the square of the hardness versus inverse indent depth, as recommended in the Nix-Gao Model [24]. This transition depth was determined to be approximately 400 nm. In order to minimize errors associated with low indentation depths and obtain good statistics, hardness and elastic modulus changes were calculated across all indents averaged from a 200-400 nm indentation depth.

Typical surface analysis was conducted using secondary electron detection mode in a Zeiss Gemini Scanning Electron Microscope to examine the effect of irradiation and nanoindentation on sample surfaces.

TEM cross-sectional foils were prepared using a FEI V400ACE Focused Ion Beam to create samples that were approximately 15 μm long by 10 μm deep with a viewing thickness of approximately 50-100 nm. The final polish on these samples were done using a 2 kV, 8 pA probe to help eliminate any residual damage/amorphous regions created during initial milling. An FEI Tecnai Transmission Electron Microscope was used to image defects in select samples. For the initial analysis, a traditional two-beam condition was used with a beam direction of approximately $\langle 11\bar{2}0 \rangle$, as determined by electron diffraction and Kikuchi patterns. This allowed for imaging along the approximate diffraction vectors (*g*) of $\langle 0001 \rangle$ and $\langle 1\bar{1}00 \rangle / \langle 01\bar{1}0 \rangle$, corresponding to the characteristic basal and prismatic directions of the HCP crystal structure. As no large voids were observed in the traditional two-beam imaging condition, under- and over-focus imaging was used to search for the existence of any small voids in the materials [25, 26].

Results

Figures 2, 3, and 4 show as-irradiated sample surfaces at the four irradiation conditions for Ti_3AlC_2, Ti_2AlC, and Ti_3SiC_2 respectively. From Figs. 2 and 3, it can be seen that both of the aluminum based MAX phases show significant surface cracking at both doses following irradiation at 400˚C, while no significant cracking was observed at both doses following irradiation at 700˚C. In contrast, the surface images of the silicon based MAX phase shown in Figure 6.3 show no significant surface cracking at either the low or high temperature irradiation conditions for either dose.

The Ti_3AlC_2 30 dpa -700˚C (Figure 2(d)) sample had significant contamination build up on the surface of the sample, believed to be hydrocarbon formation caused from outgassing of silver paste used to fasten the sample to the substrate for the ion irradiations. Cross section analysis showed that the contaminant film was 100-200 nm at its thickest. This surface contamination is believed to be responsible for slight difference between the Ti_3AlC_2 10 dpa -700˚C and 30 dpa -700˚C diffraction patterns and the unexpected decrease in hardness of the Ti_3AlC_2 30 dpa -700˚C data point discussed later in this section.

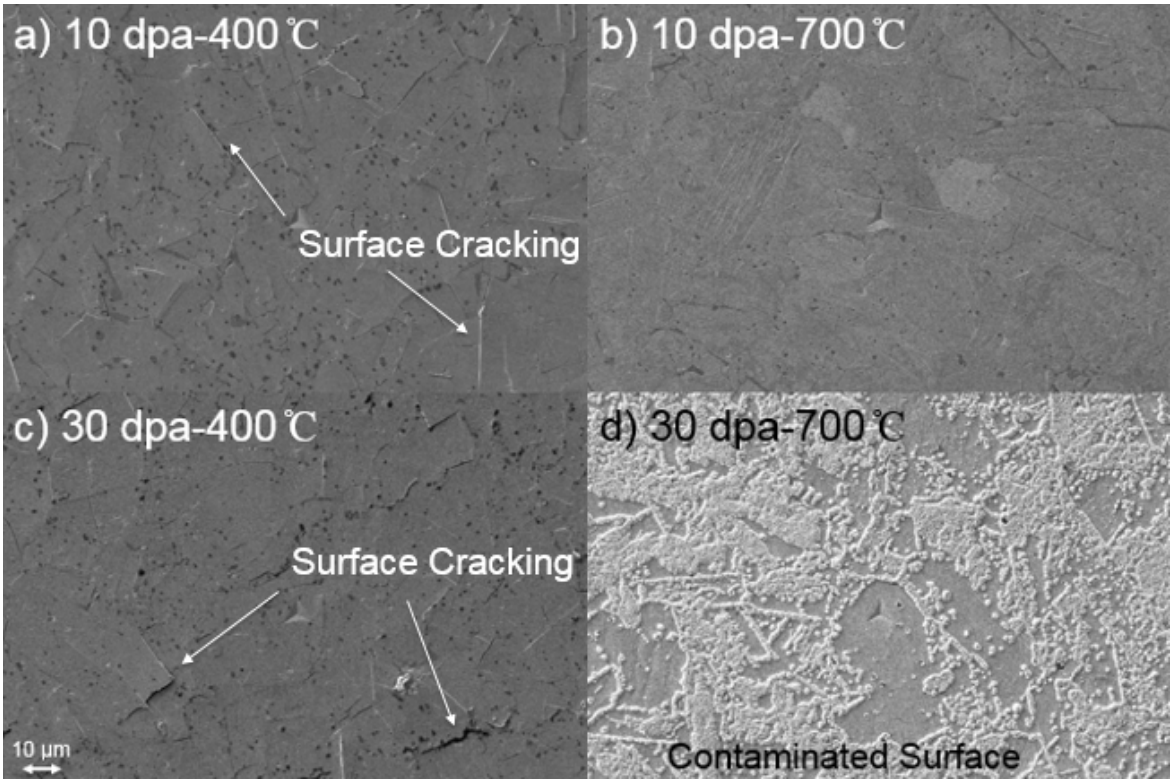

Figure 2 SEM surface imaging on Ni ion irradiated Ti_3AlC_2 for (a) 10 dpa-400˚C, (b) 10 dpa -700˚C, (c) 30 dpa-400˚C, and (d) 30 dpa-700˚C irradiation conditions.

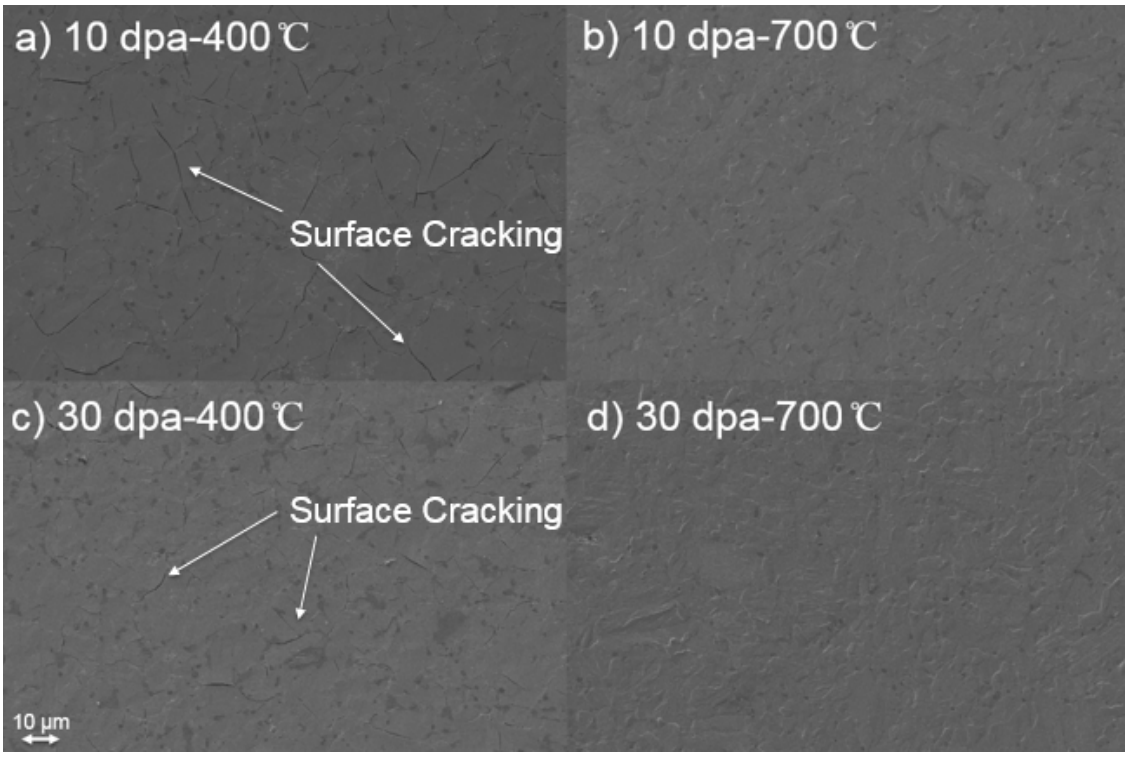

Figure 3 SEM surface imaging on Ni ion irradiated Ti_2AlC for (a) 10 dpa-400˚C, (b) 10 dpa-700˚C, (c) 30 dpa-400˚C, and (d) 30 dpa-700˚C irradiation conditions.

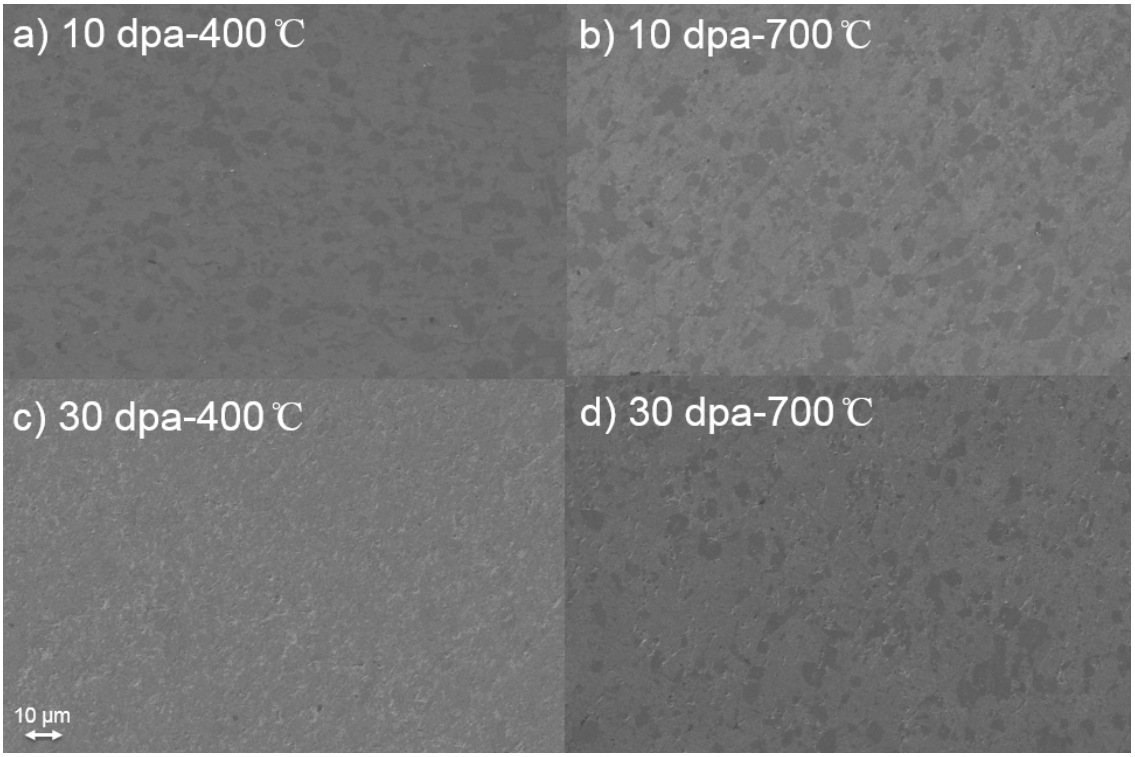

Figure 4 SEM surface imaging on Ni ion irradiated Ti_3SiC_2 for (a) 10 dpa-400˚C, (b) 10 dpa-700˚C, (c) 30 dpa-400˚C, and (d) 30 dpa-700˚C irradiation conditions.

The degree of surface cracking was quantified for the irradiated samples to determine if there was any discernable dependence of cracking on material composition, dose, or temperature. Randomly oriented lines were drawn across surface images. The number of crack intersections were counted for a large number of lines and divided by the total line length to provide a quantitative measure of the cracked grain boundary area per unit volume (S_v) using the formula S_v=2N where N is the average number of cracked grain boundary intersections per unit length of randomly drawn surface lines [27]. This crack density parameter does not take into account other crack features that might have an impact on structural integrity, such as average crack length, but was used to quantify overall cracking severity. The measured S_v values for samples irradiated at 400˚C are summarized in Table 2. As can be seen, there is no discernable difference in the linear crack densities between the same aluminum MAX phase materials at different doses at 400˚C, though the Ti_2AlC does appear to have a slightly higher crack density than the Ti_3AlC_2. As noted earlier, surface cracking was not observed in Ti_3SiC_2 for either dose at 400˚C, and no surface cracking was observed in any of the three materials irradiated at either dose at 700˚C.

Table 2 Irradiation-induced surface cracking per unit volume in Ti_3AlC_2 and Ti_2AlC irradiated at 400˚C.

Condition	S_v (1/μm)	Std. Dev.
Ti_3AlC_2-10 dpa-400˚C	1.52E-01	9.72E-03
Ti_3AlC_2-20 dpa-400˚C	1.49E-01	8.25E-03
Ti_2AlC-10 dpa-400˚C	2.13E-01	1.33E-02
Ti_2AlC-30 dpa-400˚C	1.97E-01	1.63E-02

The GXRD patterns for irradiated Ti_3AlC_2 at low dose (10 dpa) and high dose (30 dpa) can be seen in Figure 5, where (a, d) denotes low temperature (400˚C), (b, e) high temperature (700˚C), and (c, f) pristine conditions. The graphics are presented such that, going from bottom to top, it can be seen there is a significant temperature dependence on the disruption of the diffraction patterns. It can also be seen in Figure 5 that there is very little variation in the irradiated diffraction patterns with increasing dose from 10 dpa to 30 dpa, with the sole exception of the high dose, high temperature (30 dpa-700˚C) sample that was believed to have an artifact associated with surface contamination accrued during the irradiation. Additionally, the deduced lattice parameter changes for all four irradiation conditions yielded virtually identical results for samples irradiated at the same temperature but different doses. For these reasons, and in order to save time and cost, the remaining two materials, Ti_2AlC and Ti_3SiC_2, were only analyzed using GXRD at the high dose condition (30 dpa), with only the high dose Ti_3AlC_2 patterns being used for comparison. The GXRD patterns for Ti_2AlC and Ti_3SiC_2 at (a) 30 dpa-700˚C, (b) 30 dpa-700˚C, and (c) pristine conditions are shown in Figs. 7 and 8 respectively.

Editor's note: There is no Figure 6 in this section.

In all cases, the ion irradiation resulted in augmentation of the diffraction pattern through reduction of the peak heights, broadening, and shifting of the peak locations. In all three materials, there is significantly less disruption of the diffraction pattern at the 30 dpa-700˚C condition then at the 30 dpa-400˚C condition. Consequently, there are only slight differences in the pristine and 30 dpa-700˚C diffraction patterns for all three materials, with the Ti_3AlC_2 30 dpa-700˚C sample exhibiting the most change. Further examinations of the diffraction patterns shows that the Ti_3SiC_2 irradiated samples appear to show the least disturbance due to irradiation, with very little peak shift and only slight peak reduction and broadening. Consequently, only minor diffraction peaks are lost for this material at the 30 dpa-400˚C condition. In stark contrast, both aluminum based MAX phases appear to have suffered significant damage at the 30 dpa-400˚C irradiation. Only the largest diffraction peaks are still visible in Ti_2AlC and both the both aluminum MAX phases exhibit peaks that are not prevalent in the pristine samples, suggesting large shifts and/or emergence of new peaks.

Manipulation of the ICSD diffraction pattern peak positions to match the observed data using Highscore Plus yielded nominal lattice parameter changes for each material. A summary of these calculated values can be seen in Table 3.

In all three MAX phases, there was a pronounced increase in the c-LP at the 30 dpa-400˚C irradiation condition, with a less significant increase of the c-LP in the Ti_3AlC_2 and only minimal change for the Ti_2AlC, and Ti_3SiC_2 at the 30 dpa-700˚C irradiation condition. At the 30 dpa-400˚C condition, the Ti_2AlC exhibited the highest c-LP swelling, with an increase from 13.41(5) Å to 13.74(8) Å, an increase of approximately 2.46%. The Ti_3SiC_2 exhibited the least amount of c-LP swelling for irradiation at 400˚C, with an increase of 17.65(4) Å to 17.72(6) Å, corresponding to a relative increase of approximately 0.40%. For the 30 dpa-400˚C irradiation condition, Ti_3AlC_2 fell in between with an increase of 18.54(6) Å to 18.74(9) Å, or 1.08%. For the 30 dpa-700˚C condition, only the Ti_3AlC_2 exhibited lattice parameter swelling, which was limited to 0.38%, from 18.54(6) Å to 18.61(3) Å. Both the Ti_2AlC, and Ti_3SiC_2 exhibited slight contraction from pristine c-LP values at the 30 dpa-700˚C condition.

With respect to the a-LP, both aluminum MAX phases exhibit a slight a-LP reduction at the 30 dpa-400˚C condition with minimal change at the 30 dpa-700˚C condition, while the silicon based MAX phase exhibits a slight a-LP increase at both irradiation conditions. The Ti_2AlC shows the most a-LP contraction at the 30 dpa-400˚C irradiation condition, decreasing from 3.061(8) Å to 3.04(1) Å, a change of 0.69%. The Ti_3AlC_2 exhibits a less exaggerated reduction, going from 3.0735(7) Å to 3.065(5) Å, a 0.28% change at the 30 dpa-400˚C condition. Both aluminum MAX phases exhibit only slight change at the 30 dpa-700˚C irradiation condition (absolute change of 0.2% or less). The silicon base MAX phase exhibits a slight increase in the a-LP at both the 30 dpa-400˚C and 30 dpa-700˚C irradiation conditions, going from 3.059(4) Å to 3.069(3) Å and 3.067(3) Å, a 0.33% and 0.26% respective increase. A plot of both the relative (a) c-LP and (b) a-LP shifts post irradiation can be seen in Figure 9. It should be noted that large differences in c-axis and a-axis swelling can produce pronounced strains at randomly oriented grain boundaries and can result in grain boundary cracking depending on the magnitude of anisotropic swelling and material parameters.

Table 3. Irradiation-induced structural changes in Ti_3AlC_2, Ti_2AlC, and Ti_3SiC_2 for irradiation up to 30 dpa at 400˚C and at 700˚C.

Condition	a-LP (Å)	Δa-LP (%)	c-LP (Å)	Δc-LP (%)
Ti_3AlC_2-Pristine	3.0735(7)	-	18.54(6)	-
Ti_3AlC_2-10 dpa-400˚C	3.068(6)	-0.18	18.74(7)	1.08
Ti_3AlC_2-10 dpa-700˚C	3.070(1)	-0.11	18.60(1)	0.32
Ti_3AlC_2-30 dpa-400˚C	3.065(5)	-0.28	18.74(9)	1.08
Ti_3AlC_2-30 dpa-700˚C	3.076(3)	0.08	18.61(3)	0.38
Ti_2AlC-Pristine	3.061(8)	-	13.41(5)	-
Ti_2AlC-30 dpa-400˚C	3.04(1)	-0.69	13.74(8)	2.46
Ti_2AlC-30 dpa-700˚C	3.055(7)	-0.20	13.38(5)	-0.22
Ti_3SiC_2-Pristine	3.059(4)	-	17.65(4)	-
Ti_3SiC_2-30 dpa-400˚C	3.069(3)	0.33	17.72(6)	0.40
Ti_3SiC_2-30 dpa-700˚C	3.067(3)	0.26	17.61(3)	-0.23

Numbers in parentheses represent one standard deviation of the last significant digit.

In order to obtain a quantitative estimation of the critical differential strain required for grain boundary cracking, the analytical technique developed by Clarke et al. in their 1964 studies on grain boundary cracking in BeO was used [28]. Their analysis considered the misfit strain introduced at grain boundaries from anisotropic lattice expansion that led to grain boundary cracking. Spontaneous cracking is predicted to occur for misfit strains above a critical value given by Eq. (5), where the critical differential strain (ε) is related to the grain boundary surface energy in the absence of anisotropic strain (γ), the elastic modulus (E), and the average grain diameter ($2l$).

$$\varepsilon \sim \left(\frac{24\,\gamma}{El}\right)^{\frac{1}{2}} \qquad (5)$$

The grain diameters were measured for each of the materials by Darin Tallman at Drexel University [17] and were independently confirmed using Electron Back Scattering diffraction in the present study. The nominal average grain diameter for Ti_3AlC_2, Ti_2AlC, and Ti_3SiC_2 were determined to be 16(6), 10(4), and 8(3) µm respectively. The elastic moduli are given in Table 1 and the grain boundary surface energy was assumed to be 1.5 N/m, a typical value for Al_2O_3. A comparison of the calculated critical differential strain and the experimental differential strains for the three materials irradiated at the two temperature conditions can be seen in Table 6. As can be seen, only the low temperature irradiated aluminum base MAX phase samples experienced differential swelling sufficient to induce grain boundary cracking (an order of magnitude larger than the predicted critical value), supporting the conclusion that anisotropic swelling is the cause of grain boundary cracking in the 400˚C irradiated aluminum MAX phases.

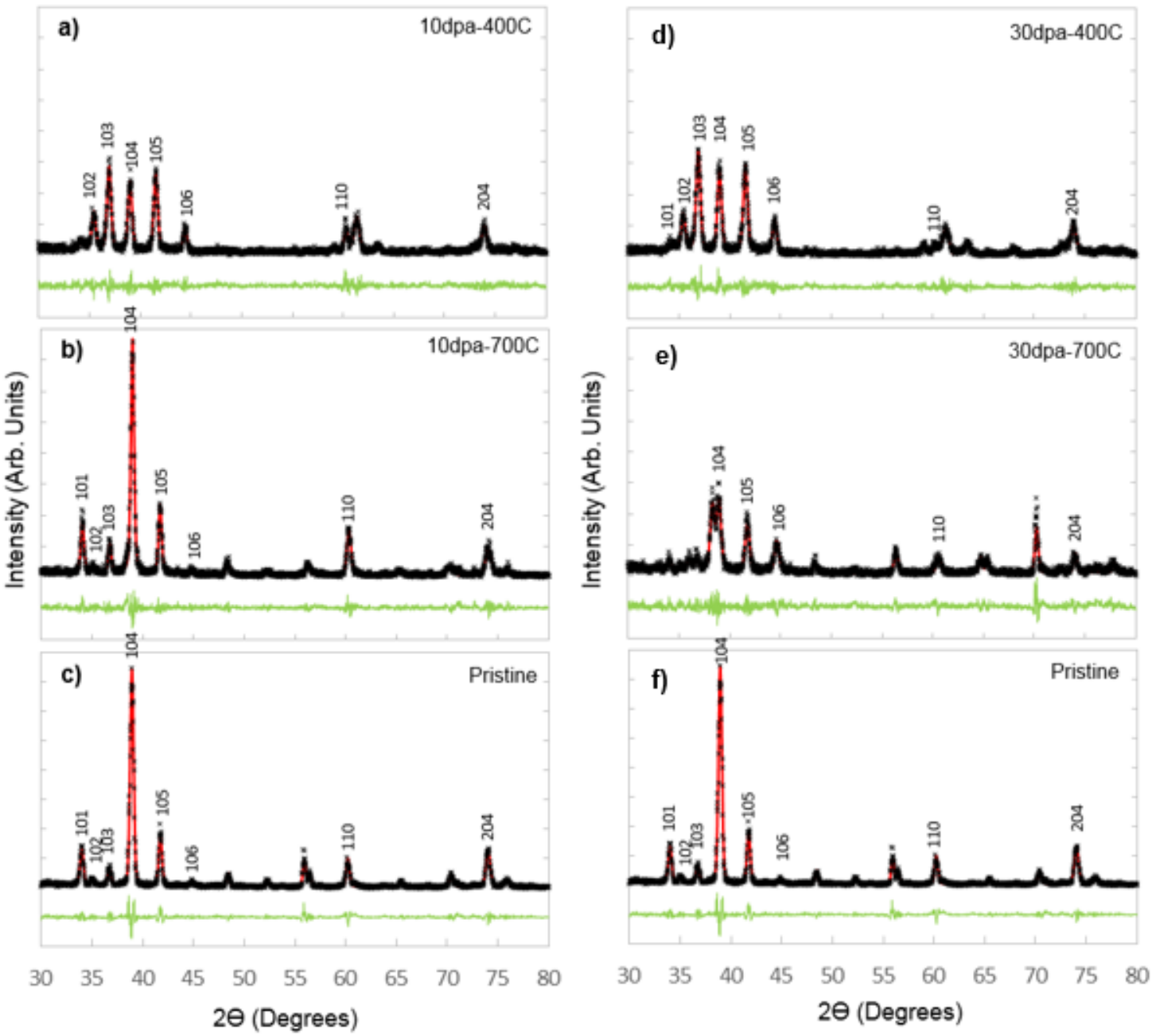

Figure 5 GXRD data of Ti_3AlC_2 irradiated to a midrange dose of 10 dpa using 5.8 MeV Ni ions at (a) 10 dpa-400˚C, (b) 10 dpa-700˚C, (d) 30 dpa-400˚C, (e) 30 dpa-700˚C, and (c&f) Pristine Ti_3AlC_2. Black data points, solid red lines, and solid green lines represent the observed data, calculated model, and the difference between the two respectively.

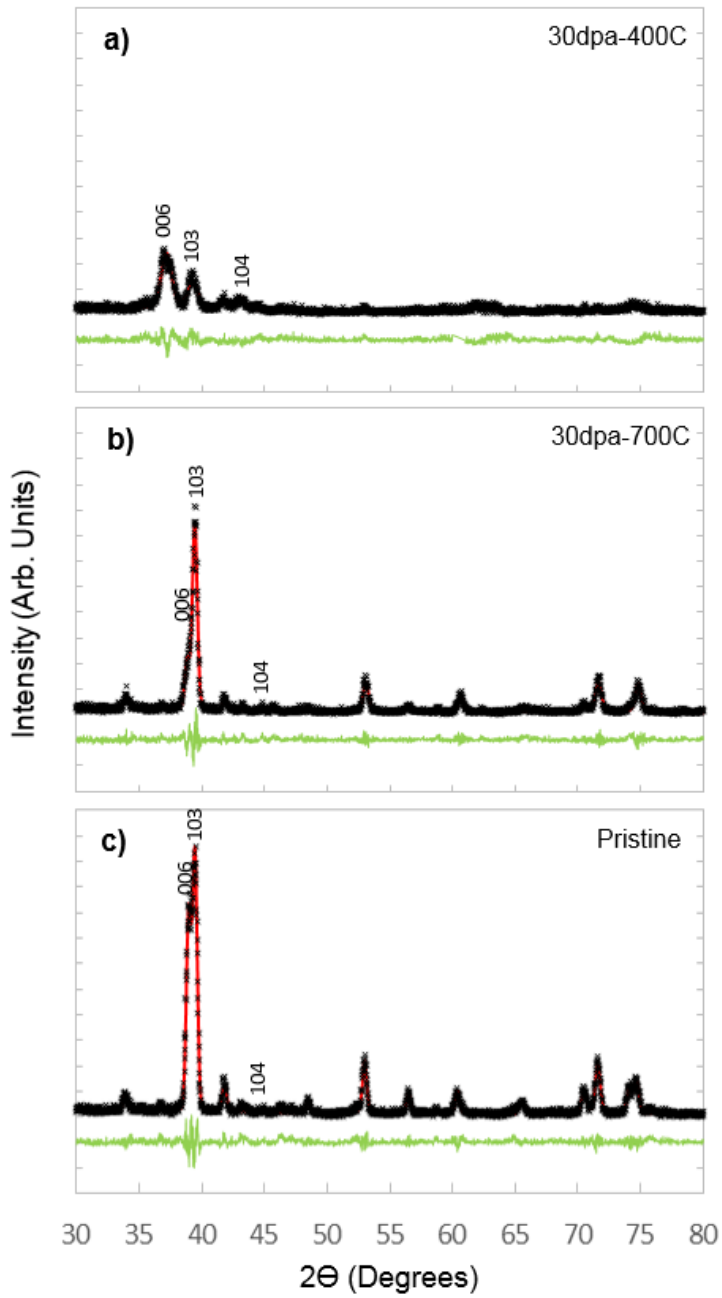

Figure 6 GXRD data of Ti_2AlC irradiated to a midrange dose of 30 dpa using 5.8 MeV Ni ions at (a) 30 dpa-400˚C, (b) 30 dpa-700˚C, and (c) Pristine Ti_2AlC. Black data points, solid red lines, and solid green lines represent the observed data, calculated model, and the difference between the two respectively.

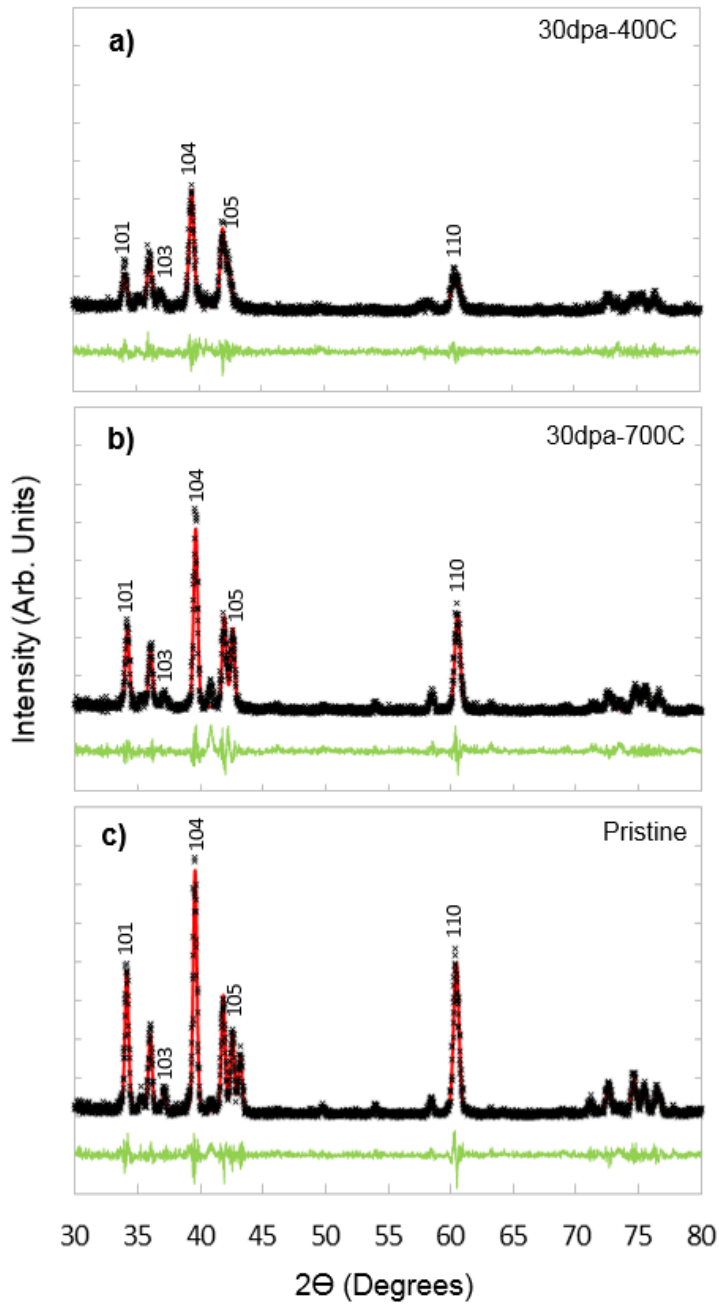

Figure 7 GXRD data of Ti_3SiC_2 irradiated to a midrange dose of 30 dpa using 5.8 MeV Ni ions at (a) 30 dpa-400˚C, (b) 30 dpa-700˚C, and (c) Pristine Ti_3SiC_2. Black data points, solid red lines, and solid green lines represent the observed data, calculated model, and the difference between the two respectively.

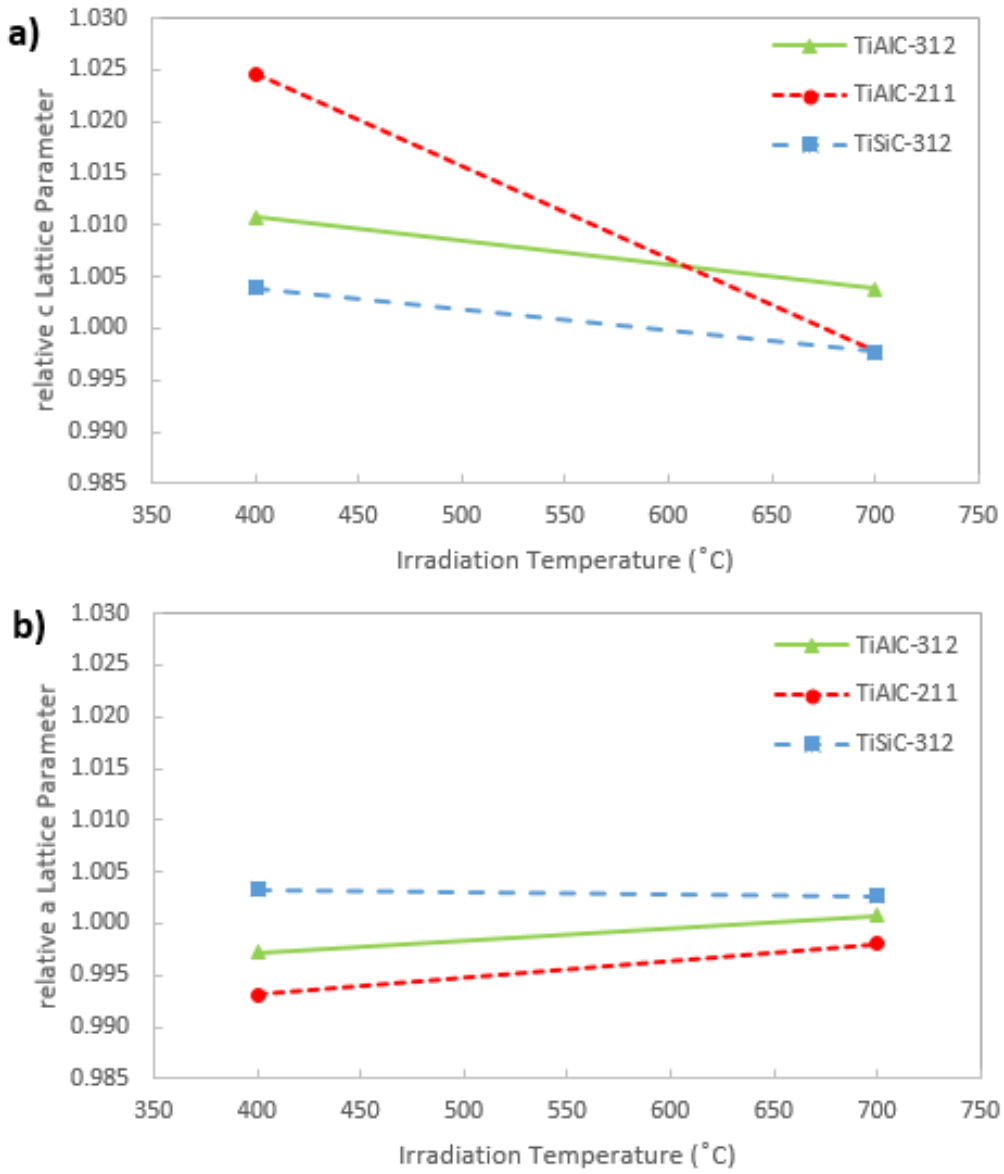

Figure 8 Temperature dependent relative lattice parameter shifts at 30 dpa midrange dose for (a) c-LP and (b) a-LP.

Table 4 Comparison of experimental differential strain to estimated critical differential strain required for grain boundary cracking.

Sample	ε at 400˚C	ε at 700˚C	ε critical
Ti_3AlC_2	1.36E-02	2.96E-03	3.89E-03
Ti_2AlC	3.15E-02	2.77E-04	5.10E-03
Ti_3SiC_2	6.97E-04	4.88E-03	5.14E-03

The evolution of hardness as a function of irradiation dose averaged over 200-400 nm for the three MAX phase materials can be seen at (a) 400˚C and (b) 700℃ in Figure 10. It can be seen that for all three materials at both 400˚C and 700℃, there is significant increase in hardness from the pristine samples to the irradiated samples, due to radiation induced defects. Of the three materials, Ti_3AlC_2 exhibits the most radiation hardening up to a maximum of approximately 1.9x for the low temperature irradiations and 1.6x for high temperature irradiations. In comparison, Ti_3SiC_2 exhibits the least amount of hardening at both the low and high temperature irradiation conditions with a maximum of approximately 1.4x and 1.2x respectively. The Ti_2AlC falls in between the other materials with a maximum relative hardening of approximately 1.6x at the low temperature condition and 1.4x at the high temperature condition. Additionally, it can be seen that there is little variation in hardness from samples irradiated at to a midrange dose of 10 dpa and those irradiated to a midrange dose of 30 dpa, for both irradiation temperatures. This suggests a saturation effect in the radiation induced hardening has occurred for a dose of 10 dpa and higher. As noted for the GXRD results in the previous section, the surface contamination of the 30 dpa- 700˚C was believed to have induced significant error on the nanoindentation results associated with this sample. As such, as dose increases from 10 to 30 dpa for Ti_3AlC_2 at the 700˚C irradiation temperature, the relative hardness of an uncontaminated sample is expected to stay constant, as is consistent with radiation hardness saturation, rather than the significant decrease as observed in the experimental data.

The effect of irradiation temperature on hardness for all three materials at a midrange dose of (a) 10 dpa and (b) 30 dpa can be seen in Figure 11. From this figure, it becomes apparent that there is significantly less hardening at an irradiation temperature of 700℃ than at an irradiation temperature of 400˚C for all three materials. This suggest a positive correlation between irradiation temperature and radiation induced hardness.

The evolution of the relative elastic modulus of the three materials as a function of irradiation dose averaged over 200-400 nm can be seen in Figure 12 for (a) 400˚C and (b) 700˚C, and as a function of irradiation temperature in Figure 13 for (a) 10 dpa midrange dose and (b) 30 dpa midrange dose. For irradiated materials there is expected to be a slight change in the elastic modulus that saturates after relatively small amounts of damage, similar to irradiation induced hardness. Upon examination, it appears that all of the irradiated samples follow this trend, with the majority of samples experiencing a slight elastic modulus increase of approximately 10%. The exception to this trend are the low temperature irradiations of the aluminum MAX phases, in which Ti_3AlC_2 exhibited little to no change in elastic modulus and Ti_2AlC exhibited a slight decrease in elastic modulus of about 6%. This behavior is indicative of a radiation induced effect not found in other samples.

SEM examination was used following indentation hardness testing to observe the surface features associated with nanoindentation. Imaging the surface indents, it was seen that for the 400˚C irradiated aluminum MAX phase surfaces (those that experienced cracking), the indenter produced significant corner cracking. For the un-cracked aluminum and all the silicon based MAX phase surfaces, the indentation did not induce corner cracking and features analogous to that of indentation on pristine MAX phase, such as slip bands/delamination and push-out, are observed [29]. Figures 14, 15, and 16 show

indents in surfaces irradiated at the (a) 10 dpa-400˚C and (b) 10 dpa-700˚C conditions in Ti_3AlC_2, Ti_2AlC, and Ti_3SiC_2 respectively.

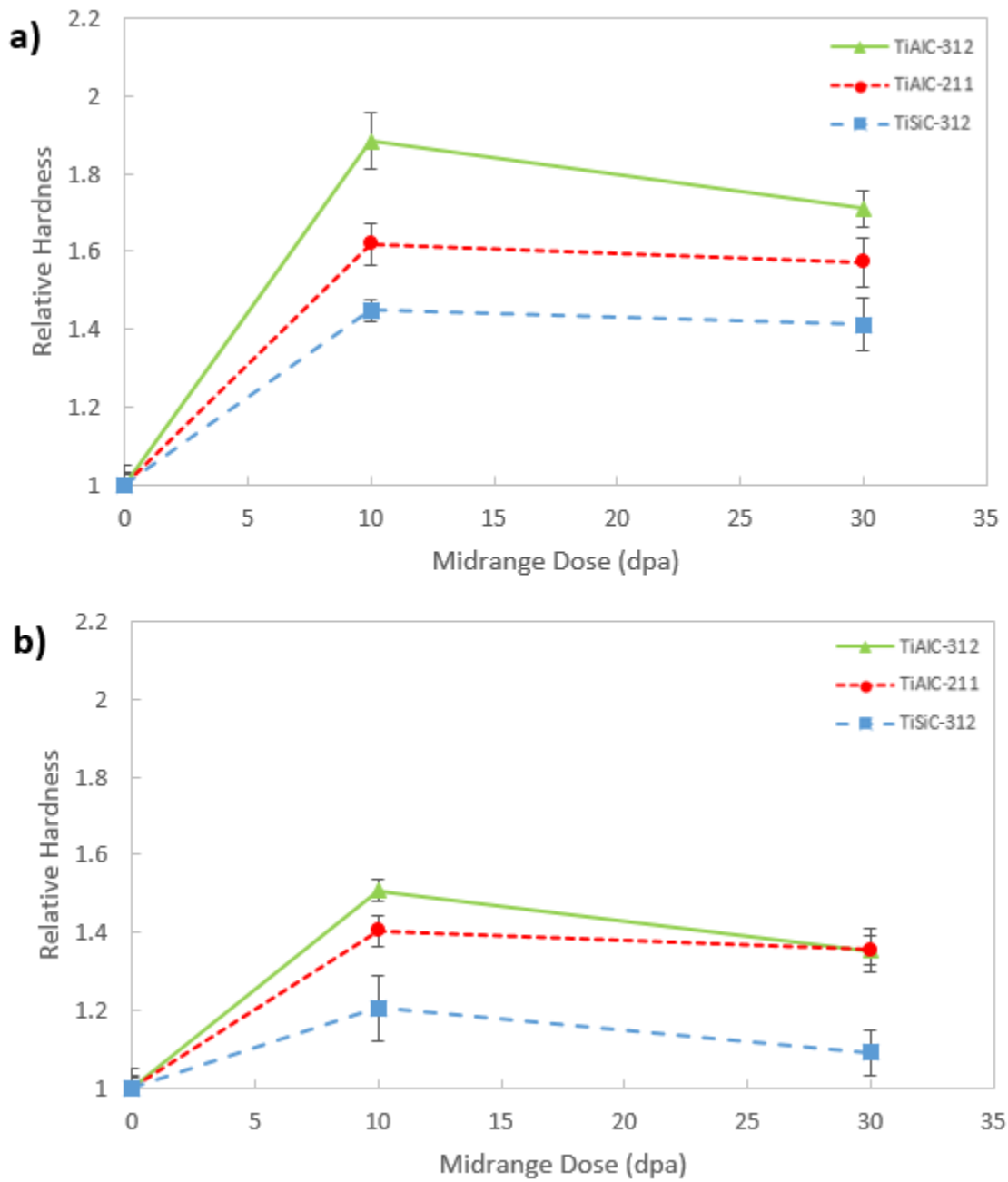

Figure 9 Normalized hardness dose dependence in irradiated Ti_3AlC_2, Ti_2AlC, and Ti_3SiC_2 by 5.8 MeV Ni ions at (a) 400˚C and (b) 700℃.

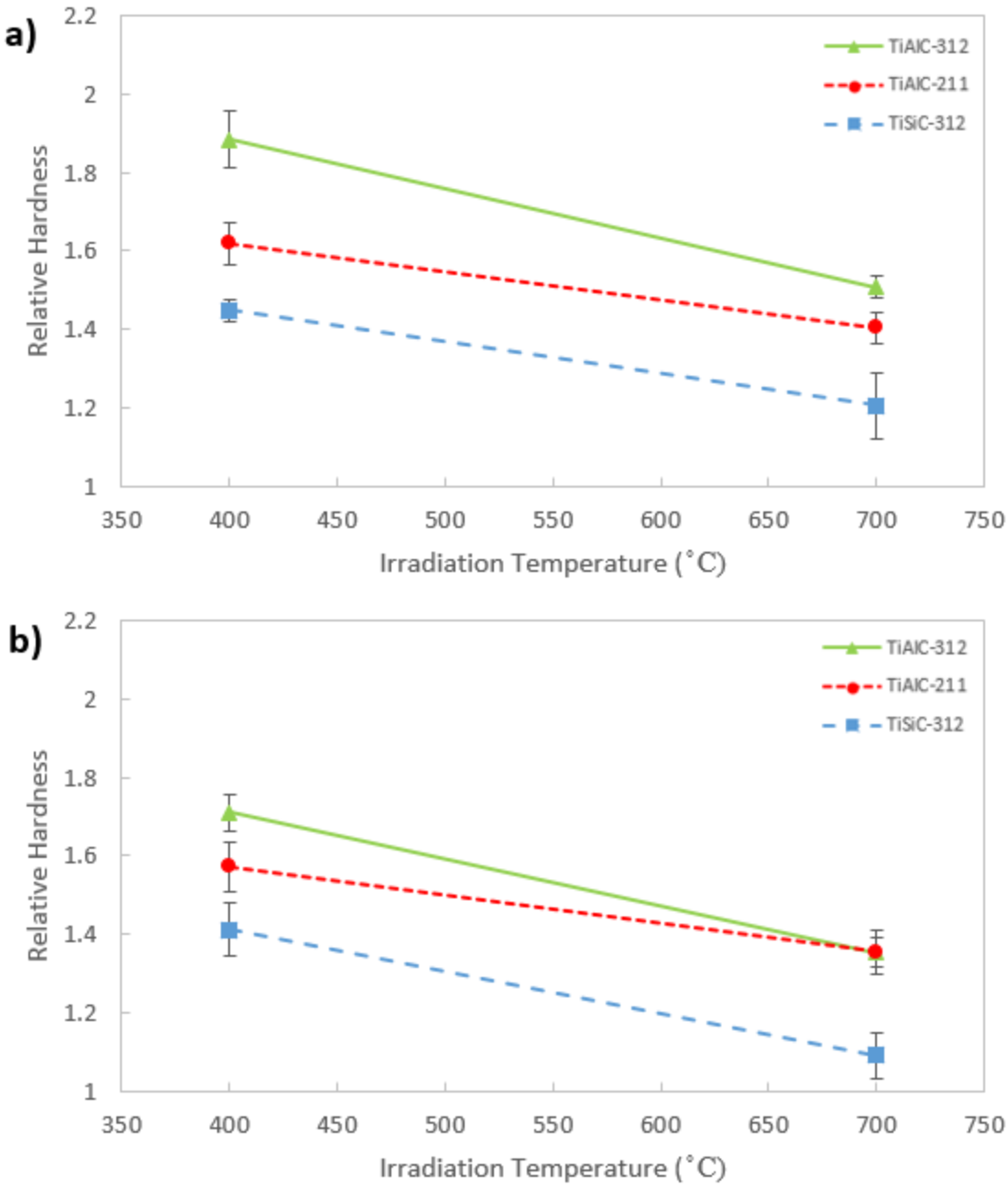

Figure 10 Normalized hardness temperature dependence in irradiated Ti_3AlC_2, Ti_2AlC, and Ti_3SiC_2 by 5.8 MeV Ni ions at midrange doses of (a) 10 dpa and (b) 30 dpa.

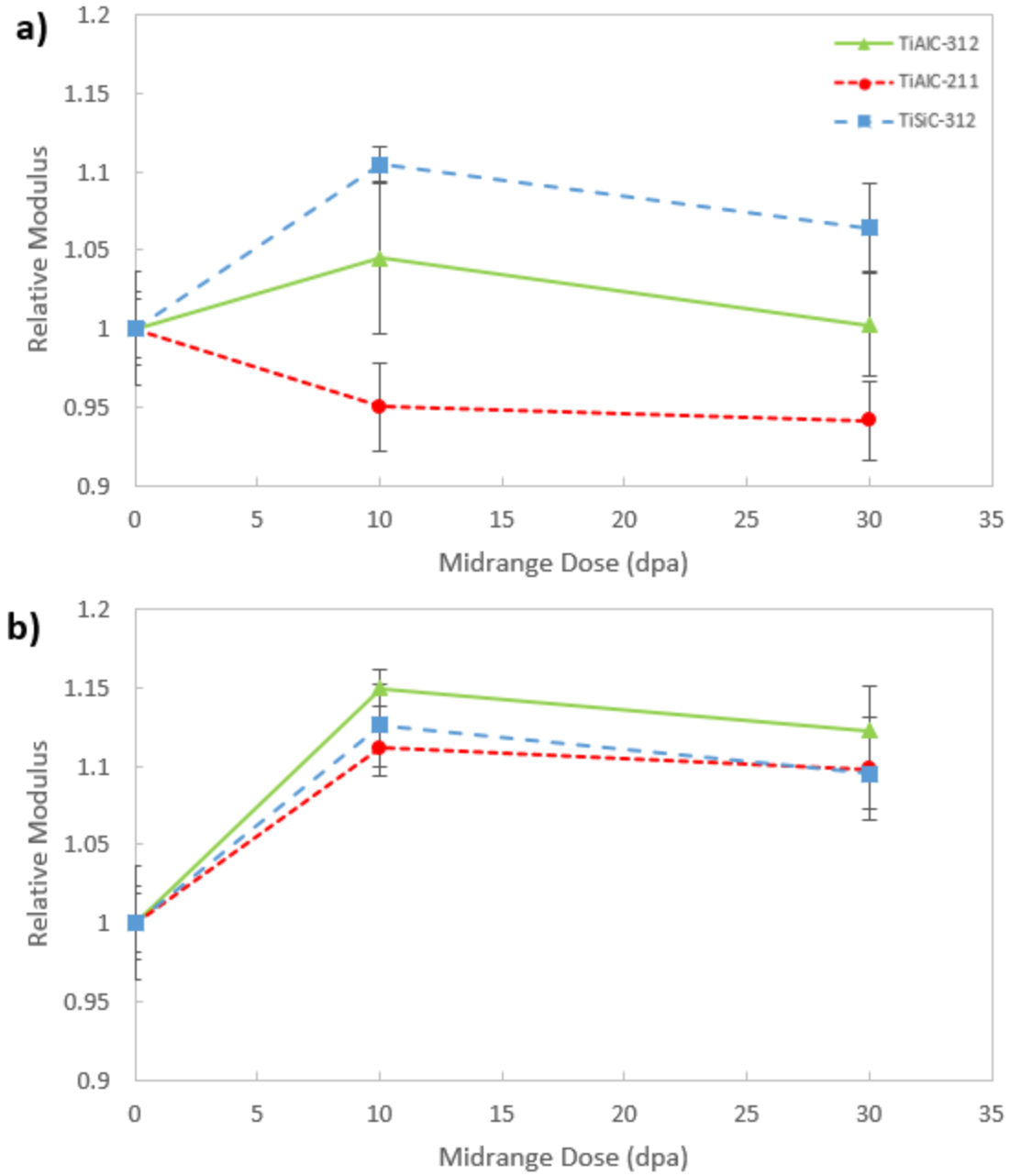

Figure 11 Normalized elastic modulus dose dependence in irradiated Ti_3AlC_2, Ti_2AlC, and Ti_3SiC_2 by 5.8 MeV Ni ions at (a) 400˚C and (b) 700˚C.

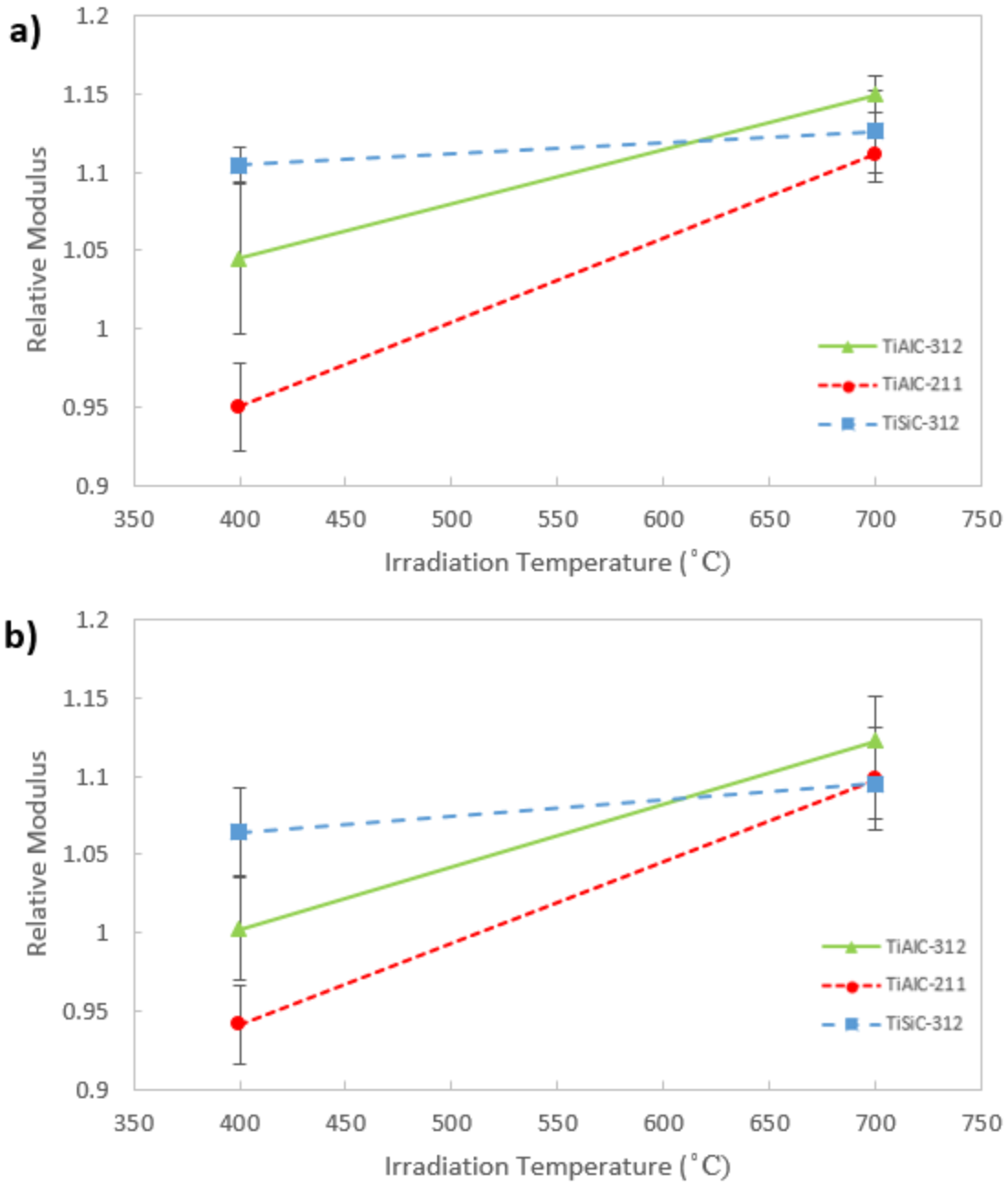

Figure 12 Normalized elastic modulus temperature dependence in irradiated Ti_3AlC_2, Ti_2AlC, and Ti_3SiC_2 by 5.8 MeV Ni ions at midrange doses of (a) 10 dpa and (b) 30 dpa.

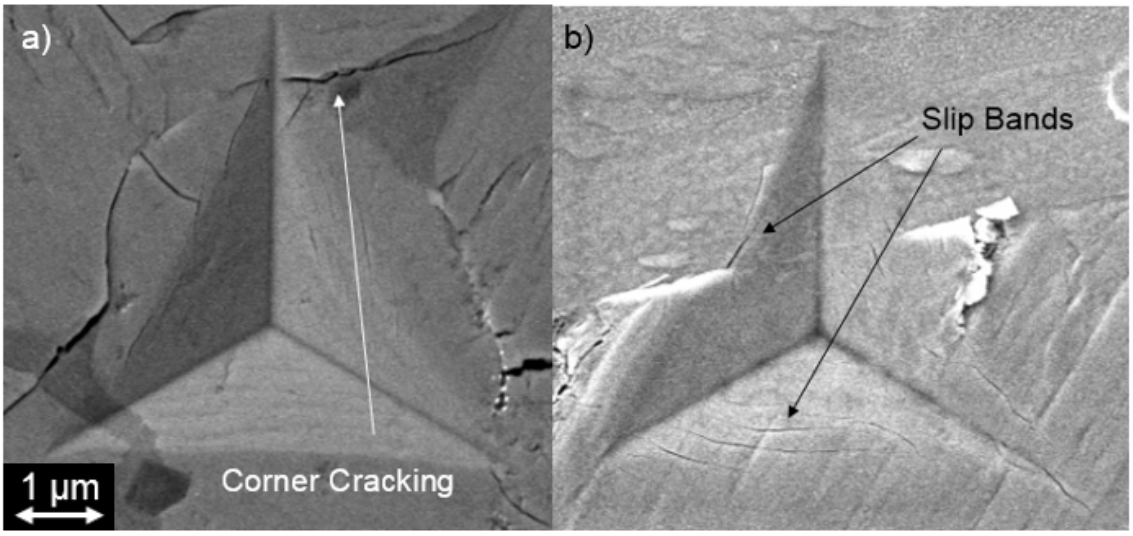

Figure 13 SEM morphology of indents on (a) 10 dpa-400˚C, and (b) 10 dpa-700˚C Ni ion irradiated Ti_3AlC_2.

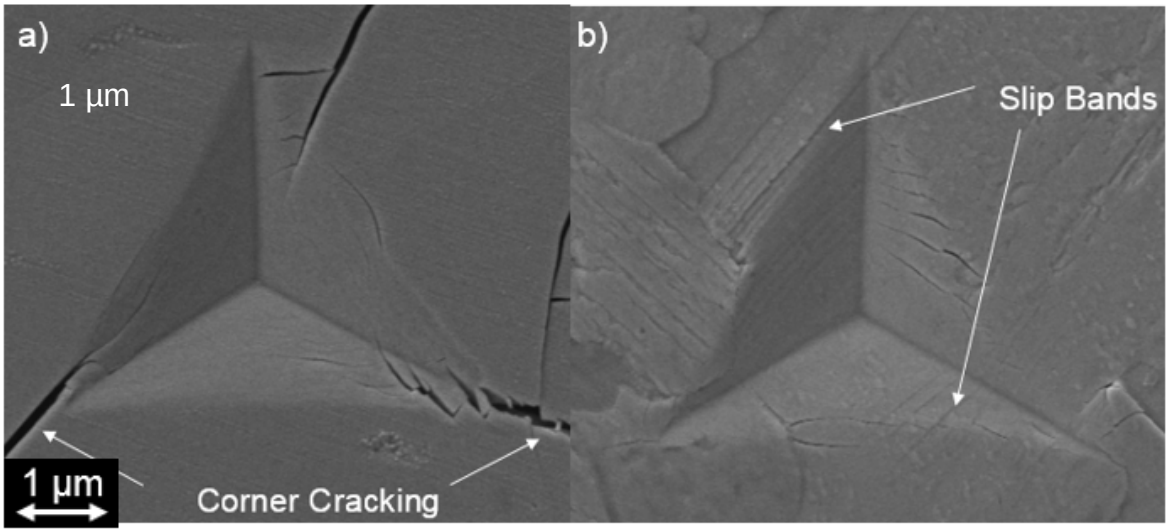

Figure 14 SEM morphology of indents on (a) 10 dpa-400˚C, and (b) 10 dpa-700˚C Ni ion irradiated Ti_2AlC.

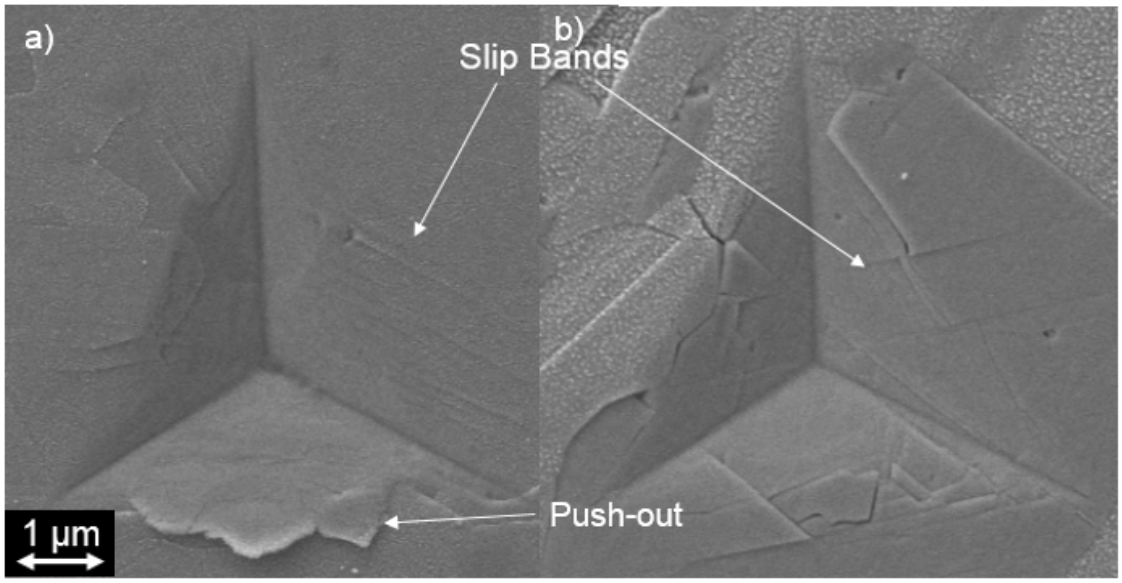

Figure 15 SEM morphology of indents on (a) 10 dpa-400˚C, and (b) 10 dpa-700˚C Ni ion irradiated Ti_3SiC_2.

TEM cross section analysis was used to examine microstructural defects in select samples. The samples chosen were those that were thought to be most relevant to the questions raised by the previous SEM surface, XRD, and nanoindentation analysis, the most important of which are why are the aluminum based MAX phases cracking at the 400˚C irradiation conditions and not cracking following 700˚C irradiation, as well as are vacancies sufficiently mobile to produce observable cavity formation in either the aluminum or silicon based MAX phase at 700˚C. Assuming that both the aluminum MAX phases would exhibit qualitatively similar microstructural evolution under irradiation (due to their qualitatively similar response in terms of lattice parameter changes, hardening, and surface cracking propensity), the samples deemed as highest priority for TEM analysis were Ti_3AlC_2 30 dpa-400˚C, Ti_3AlC_2 30 dpa-700˚C, and Ti_3SiC_2 30 dpa-700˚C.

A low-magnification TEM micrograph of the Ti_3AlC_2 30 dpa-400˚C cross-section foil and SAED results for the underlying unirradiated region (2) can be seen in Figure 17. The green arrow represents the direction of ion irradiation, which penetrated to a depth of approximately 3 µm, as displayed by the white line denoting the separation of the irradiated area and non-irradiated bulk. This is consistent with SRIM ion penetration depth calculations provided above. SAED was performed on the unirradiated region (2), well beyond the range of the ions (displayed as an inset in the upper right of Figure 17), in order to determine both the phase and orientation of the grain. Comparing experimental and ICSD diffraction pattern spacing, the grain was confirmed to be the nominal Ti_3AlC_2 phase and the beam direction was determined to be ~$\langle 11\bar{2}0 \rangle$. This low magnification analysis was completed again for both the 30 dpa-700˚C Ti_3AlC_2 and Ti_3SiC_2 samples.

Subsequently, standard two-beam conditions were used to obtain bright field and dark field images using the $\langle 0001 \rangle$ (basal) and $\langle 1\bar{1}00 \rangle$ (prism) diffraction vectors for both the unirradiated (2) and irradiated (1) regions of Ti_3AlC_2 irradiated to 30 dpa at 400˚C, as shown in Figs. 18 and 19 respectively. It is important to note that the irradiated region (1) was analyzed at a depth of ~1.5 µm, corresponding to the nominal midrange dose of 30 dpa. As can be seen in both the $\langle 0001 \rangle$ and $\langle 1\bar{1}00 \rangle$ g vectors in Figure 18, a low density of large defect clusters typical of unirradiated materials exist in the pristine region. On the contrary, for both g vectors in the 400˚C irradiated region shown in Figure 19, there is a large density of "black spots" or small defect clusters, with a distinct lack of voids (the latter was confirmed using under- and over-focusing techniques). The very high density of defect clusters visible in these images suggest a saturation of interstitial point defect clusters in the irradiated area induced through nuclear displacements.

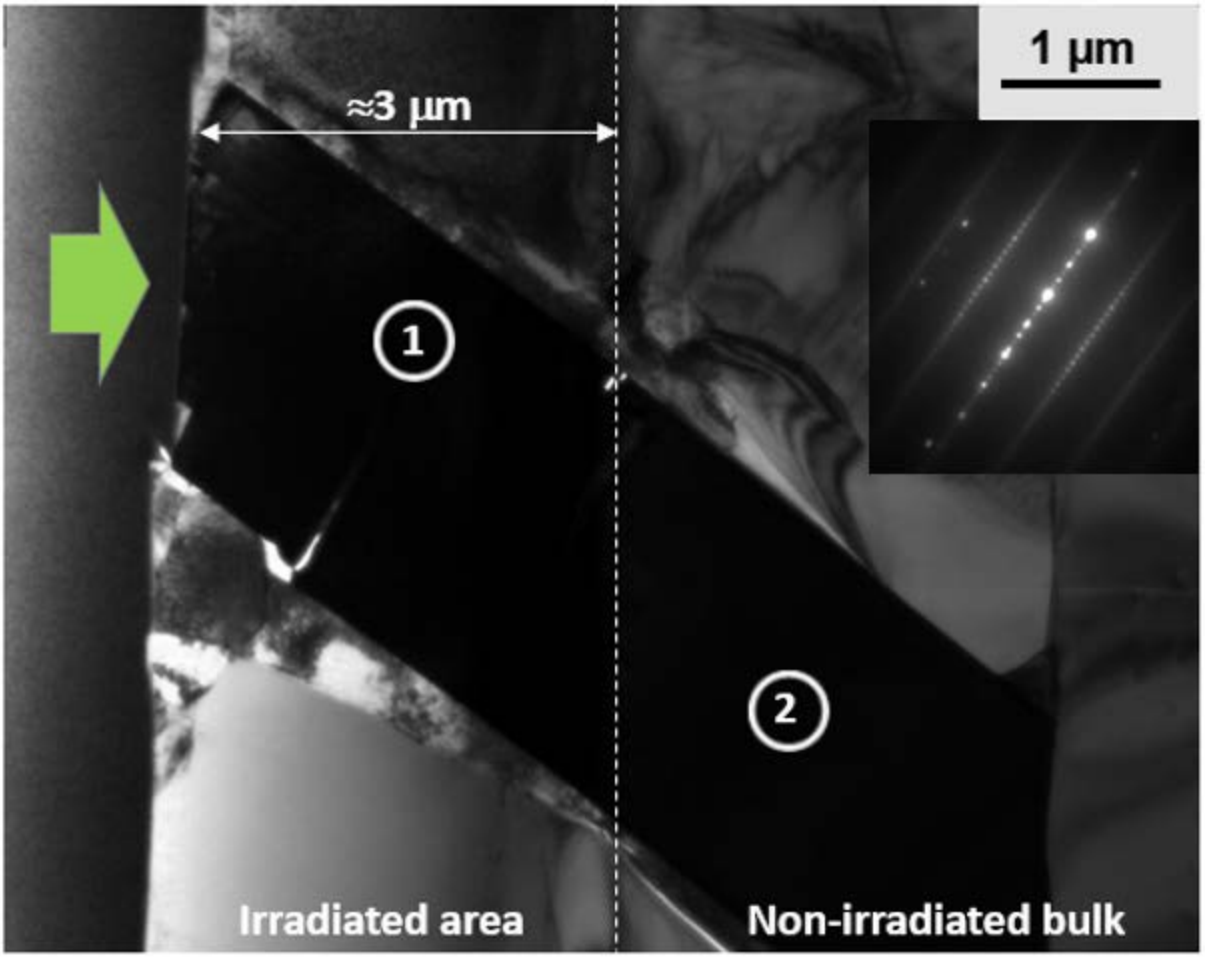

Figure 16 Cross-sectional TEM micrograph of the full Ti_3AlC_2 foil irradiated to 30 dpa at 400˚C using 5.8 MeV Ni ions, with ion direction denoted by the green arrow. The dashed white line denotes the transition depth between the ion irradiated area and the non-irradiated bulk. Region 1 denotes the selected area for ion radiation damage characterization and Region 2 denotes the selected area for pristine crystal characterization. SAED pattern for the pristine crystal can be seen in the upper right-hand corner.

Standard two-beam conditions were also used to obtain bright field and dark field images for $\langle 0001 \rangle$ (basal) and $\langle 1\bar{1}00 \rangle$ (prism) diffraction vector directions for Ti_3AlC_2 and Ti_3SiC_2 irradiated to a midrange dose of 30 dpa at 700˚C, shown in Figs 20 and 21. Again, under- and over-focus showed a distinct lack of voids, suggesting that vacancy mobility is limited in both the aluminum and silicon based MAX phase at 700˚C (or else void nucleation and growth is otherwise inhibited). However, contrary to the 400˚C irradiated Ti_2AlC, the irradiated microstructures did not contain a large density of small, point defects, but instead consisted of a lower density of large defect clusters for both the $\langle 0001 \rangle$ and $\langle 1\bar{1}00 \rangle$ diffraction vectors. In the Ti_3AlC_2, these grouped defect clusters appeared to form a hatched or diamond pattern for g=$\langle 0001 \rangle$ and a striped pattern for g=$\langle 0001 \rangle$ $\langle 1\bar{1}00 \rangle$. Upon inspection, the defects appear to be comprised of smaller basal defects that coalesce in a stacking sequence at $\pm$ 35 degree angles from the basil direction. The fact that these defects can also be seen for the prism zone axis suggest a prismatic component as well. Full characterization of these defect clusters is needed before any definitive conclusions as to their nature can be draw, but the general features of significantly coarser defect cluster microstructure suggest a higher mobility of interstitial defects at this higher irradiation temperature.

Similar to the 700˚C irradiated Ti_3AlC_2, the Ti_3SiC_2 irradiated microstructure did not contain a large density of small, point defects, but instead consisted of a lower density of larger defect clusters at both

the basal and prism viewing zone axis. However, these grouped defects did not form similar self-organized patterns seen in the Ti_3AlC_2, but instead exhibited what appears to be large stacking faults along the basal plane and dislocation loops along the prism axis. Again, full characterization of these defect clusters is still needed before any definitive conclusions as to their nature can be draw, but the general irradiation damage seen in Ti_3SiC_2 appears to be less pronounced than that observed in Ti_3AlC_2, and is consistent with previous results.

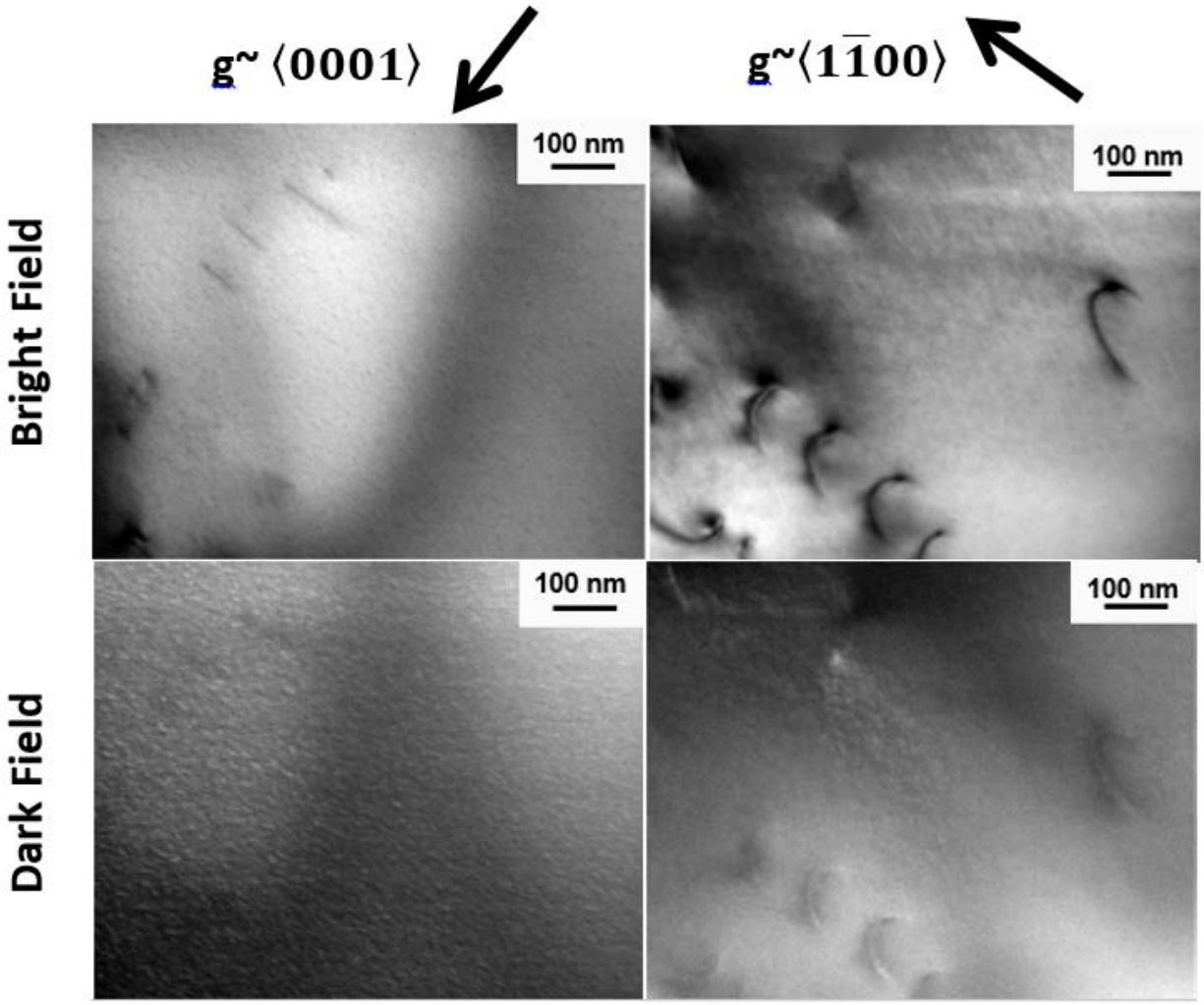

Figure 17 High magnification bright field and dark field cross-sectional TEM micrographs of pristine Ti_3AlC_2 (region 2). The basal and prism diffraction vector directions are indicated by $\langle 0001 \rangle$ and $\langle 1\bar{1}00 \rangle$ respectively.

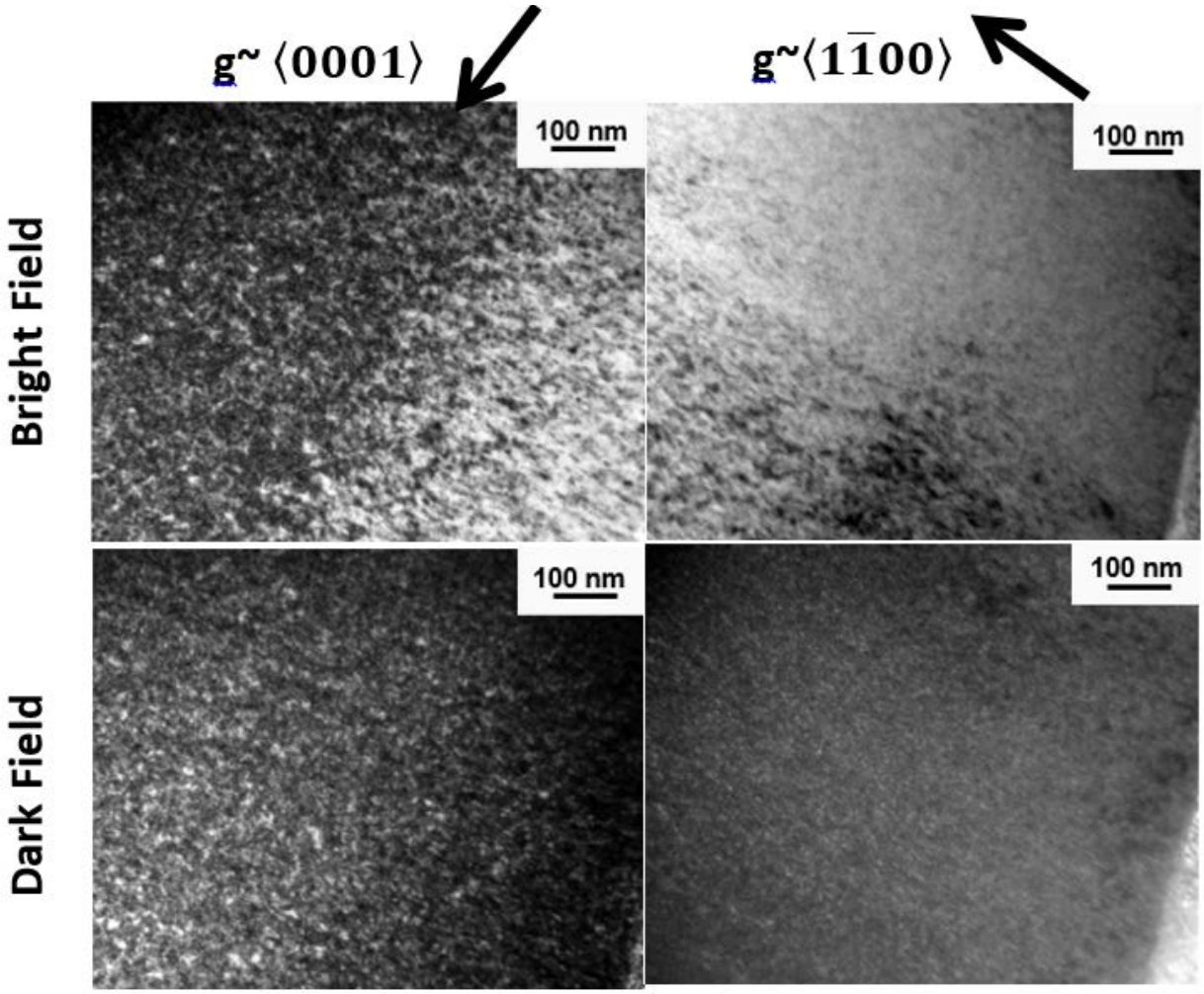

Figure 18 High magnification bright field and dark field cross-sectional TEM micrographs of 5.8 MeV Ni ions irradiated Ti_3AlC_2 to a midrange dose of 30 dpa at a temperature of 400˚C. The basal and prism diffraction vector directions are indicated by $\langle 0001 \rangle$ and $\langle 1\bar{1}00 \rangle$ respectively.

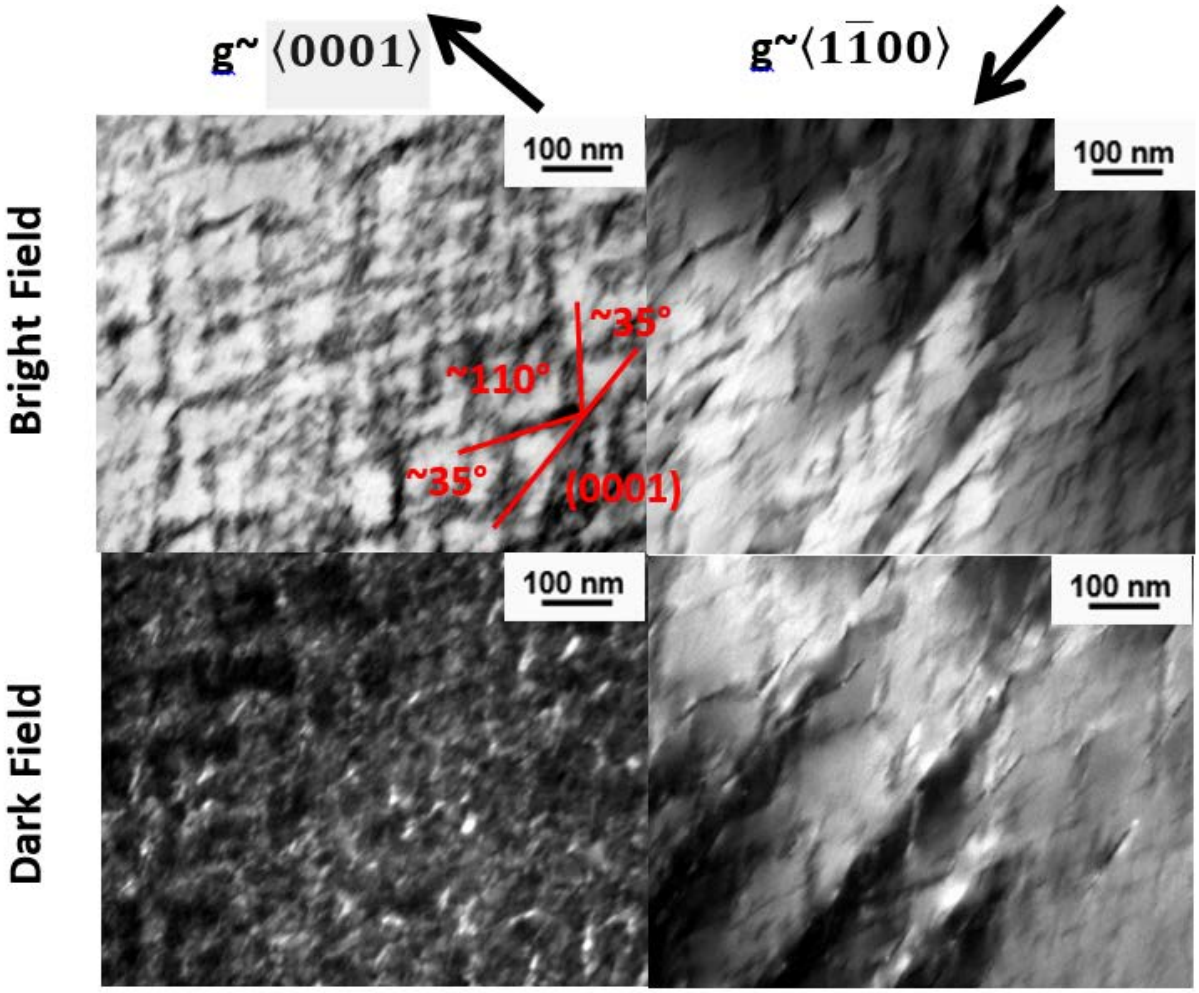

Figure 19 High magnification bright field and dark fieldcross-sectional TEM micrographs of 5.8 MeV Ni ions irradiated Ti_3AlC_2 to a midrange dose of 30 dpa at a temperature of 700˚C. The diffraction vectors are indicated by $\langle 0001 \rangle$ and $\langle 1\bar{1}00 \rangle$ respectively. The red marking show the estimated stacking sequence of small defects with respect to the basal plane.

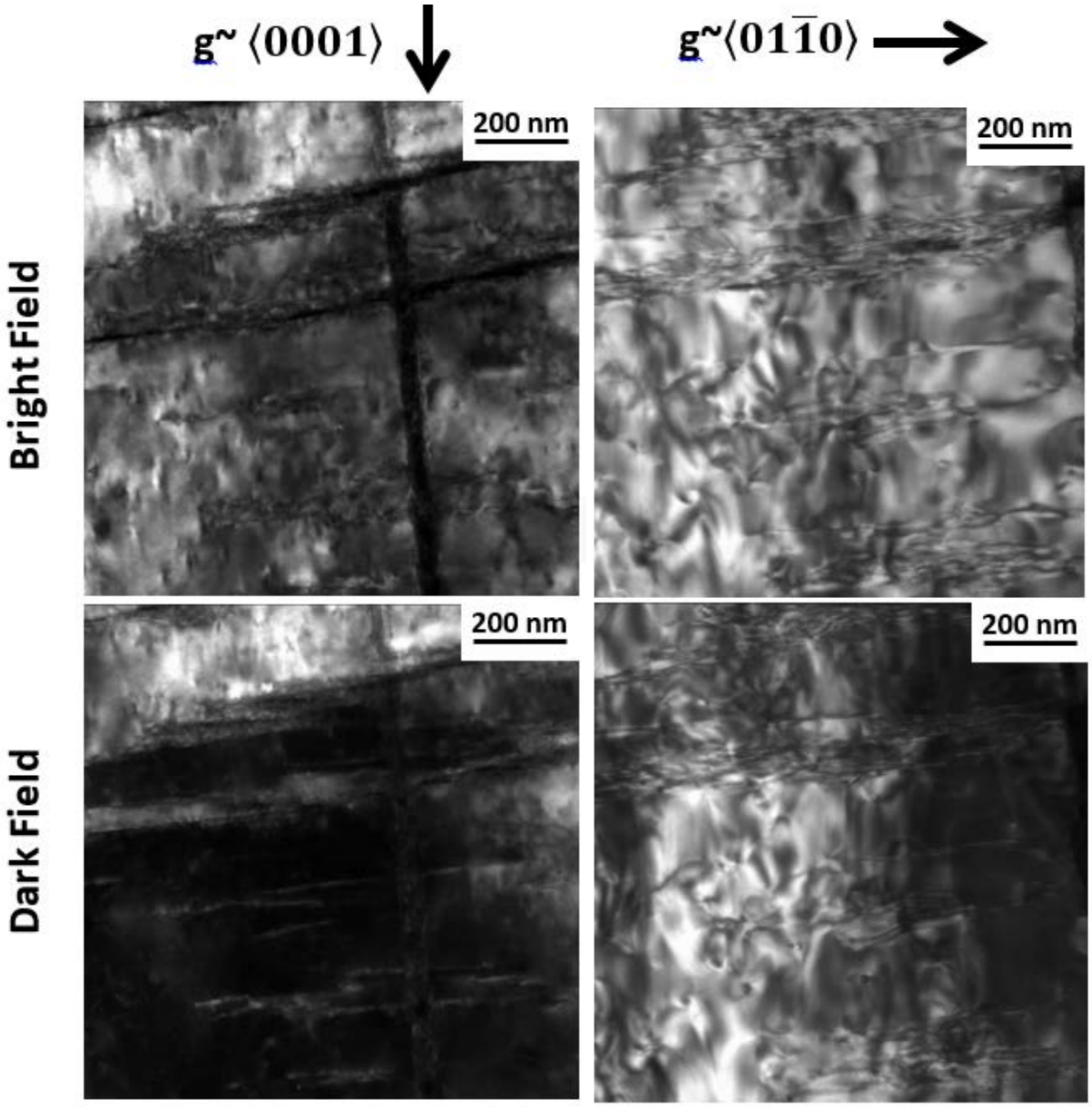

Figure 20 High magnification bright field and dark field cross-sectional TEM micrographs of 5.8 MeV Ni ions irradiated Ti_3SiC_2 to a midrange dose of 30 dpa at a temperature of 700˚C. The diffraction vectors are indicated by $\langle 0001 \rangle$ and $\langle 01\bar{1}0 \rangle$ respectively.

Discussion

The GXRD patterns collected from the ion irradiated MAX phase samples revealed a distortion of lattice parameters (LPs) under ion irradiation for all three compositions. For Ti_3AlC_2, four samples at both irradiation doses and temperatures were explored, reveling a lack of lattice parameter dilation on irradiation dose, suggesting radiation damage saturation at damage levels below 10 dpa. Contrary to the weak dose dependence, lattice dilation had a significant dependence on irradiation temperature. For all three materials, the low temperature irradiations produced the largest deviations in both the c-LP and a-LP, with all three materials experiencing an increase or swelling of their c-LP. Ti_2AlC exhibited the largest increase in c-LP, subsequently followed by Ti_3AlC_2 and lastly by Ti_3SiC_2. For a-LP at the low

temperatures, both the aluminum MAX phases showed a decrease in a-LP while the silicon MAX phase showed a slight increase in a-LP. Again, the Ti_2AlC showed the largest deviation from pristine, with both the Ti_3AlC_2 and Ti_3SiC_2 had very similar magnitudes of deviation, if with opposite signs. For most samples, irradiation at high temperatures resulted in only slight variation of LPs from their pristine values, with the exception being high temperature irradiated Ti_3AlC_2, in which there was still noticeable, though not nearly as severe, c-LP swelling. Overall, the c-LP showed more distinct deviation from pristine samples than the a-LP for all three materials at the low temperature irradiations. The results obtained from GXRD show that anisotropic swelling is the underlying cause for grain boundary cracking in the 400˚C irradiated aluminum MAX phases. The significant swelling at lower irradiation temperatures, and the subsequent decrease of swelling as irradiation temperature is increased, are consistent with what is typically observed in irradiated materials in the "point defect swelling" regime where interstitials are mobile but vacancies are immobile [15, 16]. Furthermore, the lack of dose dependence in lattice parameter swelling suggests that defect saturation is reach at some displacement level beneath the minimum 10 dpa dose analyzed in this research, again congruent with the "point defect swelling" regime, which saturates at low doses ('~0.1-1 dpa) and agrees with previous ion irradiation experiments [9-11, 17].

The increase in hardness in the irradiated MAX phases could not be attributed to oxide formation or dramatic chemical change at the sample surface, and as such, must be directly related to the formation of irradiation defects, as previously reported in other ceramics [30-33] .Furthermore, this increase in hardness is consistent with the conclusion that the materials are not being amorphized, as that would have led to a drop, rather than increase in hardness [31]. The lack of hardness change between doses at both the low temperature and high temperature irradiation conditions suggest that radiation induced hardness reaches a saturation point somewhere below the Ni ion fluence level associated with the 10 dpa midrange dose at both 400˚C and 700˚C. Additionally, the progressive recovery of induced hardness with increasing irradiation temperature suggests radiation defect recombination/annealing for all three materials. The present results are consistent with the general evolution of radiation induced hardness in the "point defect swelling" regime corresponding to temperatures between recovery Stage I (onset of interstitial migration) and recovery Stage III (onset of vacancy migration), wherein hardness is more prominent at lower irradiation temperatures and saturates after small doses [15, 16]. Additionally, it is congruent with previous nanoindentation results on MAX phase ceramics [8, 14]. In terms of elastic modulus, the majority of samples underwent a slight increase, with the exceptions being the low temperature irradiation aluminum based MAX phases, which instead underwent a slight decrease in elastic modulus. This effect has been seen in other ceramics where, after low doses, the pinning of dislocations lead to material strengthening and an increase in elastic modulus [34]. Following the SEM observations, it can be concluded that the outlying samples that experienced a decrease in elastic modulus were in fact the ones suffering from grain boundary/surface cracking, which was believed to be the direct cause for the decrease in elastic modulus. One last topic related to indentation is with respect to the damage tolerance properties of the MAX phases. Vickers or Berkovich indentation in brittle solids traditionally result in sharp cracks emanating from the corners of the indent, which is indicative of low toughness. In pristine MAX phases, instead of crack formation at corners, one typically observes delaminations or slip bands, kinking of individual grains, grain push-outs and pull-outs around the area of indentations [29].

SEM examination of indentations showed that no cracks were induced during indentation in the silicon base MAX phase at any of the four irradiation conditions or in the high temperature irradiated aluminum based MAX phases. It is far from conclusive, but the presence of characteristic sliding features in the materials that did not exhibit corner cracking shows that the MAX phases are still able to confine localized mechanical damage and are reasonably damage tolerant at those conditions, albeit to what extent is still unknown. This can be attributed to the preservation of the typical layered structure of the MAX phases, and agrees with the GXRD results wherein the most heavily disordered structures appeared to be those of the aluminum MAX phases at the low irradiation temperatures. Due to the fact that indentation induced pronounced corner cracking in the low temperature irradiated aluminum MAX phases, it can be suggested that irradiation at these conditions for these materials affected the microstructure in such a way as to decrease the damage tolerance.

The presented TEM micrographs exhibit several key features that further support the results discussed above. The appearance of a standard crystalline SAED pattern in the irradiated 30 dpa-400˚C irradiated

Ti_3AlC_2, which is arguably one of the most damaged materials confirms that crystallinity is indeed maintained in all three materials at all irradiation conditions. The high density of small defect clusters in the 30 dpa-400˚C irradiated Ti_3AlC_2 sample implies interstitials are sufficiently mobile to create small defect clusters while the lack of voids up to a dose of 30 dpa implies immobile vacancies at this temperature. This suggests that at 400˚C all three MAX phase are between recovery Stage I and Stage III, or the so called "point-defect swelling regime.

The micrographs of 30 dpa-700˚C irradiated Ti_3AlC_2 appear to show large, grouped clusters of small basal plane defects that coalesce at $\pm$ 35 degree step angles. This is analogous to "rafting" of small defect clusters that has been previously observed in other metallic materials, such as BBC iron, tungsten, and molybdenum [35], and full identification of these defect clusters will require more extensive imaging analysis. In any case, it is clear that the defect clusters are more distinct and with a lower density, leading to the conclusion that interstitials are more mobile than those at the 400˚C irradiation condition. The lack of voids implies that vacancies are still immobile at the 700˚C irradiation condition.

The micrographs of 30 dpa-700˚C irradiated Ti_3SiC_2 coincide with the results shown for Ti_3AlC_2 irradiated at the same condition in that they show larger, better defined defect clusters with a lower density. Again, these larger defects coupled with the lack of voids implies that interstitials have significantly higher mobility than vacancies at the 700˚C irradiation conditions in Ti_3SiC_2. The lack of "rafting" in the Ti_3SiC_2 could be indicative of fundamental differences in radiation response between the aluminum and silicon based MAX phase. However, full identification of these defect clusters through extensive imaging analysis is required before any conclusion can be drawn.

Overall, the micrographs of 30 dpa-700˚C irradiated Ti_3AlC_2 and Ti_3SiC_2, depicting larger, more fully formed defects with a lack of voids suggests that all materials are between recovery Stage I and Stage III at 700˚C. This region is defined by high interstitial mobility, which allows them to coalesce to form large defect structures, and the lack of void formation suggests that Stage III recovery, or vacancy mobility, has not been reached. This microstructural evidence suggests that the point defect swelling regime extends between at least 400 and 700˚C and explains why there is significantly more swelling at lower irradiation temperatures in all three materials. Additionally, these results agree with several studies that suggest amorphization (which occurs for irradiation temperatures below recovery Stage I) during irradiation of MAX phase ceramics is possible only for irradiation temperatures well below room temperature and that voids do not form below 900˚C [7-13, 17].

Concluding Summary

The family of layered carbides and nitrides known as MAX phase ceramics combine many attractive properties of both ceramics and metals due to their nanolaminate crystal structure and are promising potential candidates for application in fusion reactors. This report summarizes experimental results on the effects of energetic heavy ion irradiations on polycrystalline samples of two titanium aluminum carbides (Ti_3AlC_2, Ti_2AlC) and one titanium silicon carbide (Ti_3SiC_2). The irradiation conditions consisted of midrange ion doses between 10 and 30 displacements per atom at temperatures of 400 and 700°C, conditions relevant to application in fusion reactors, and a relatively un-explored regime for MAX phase materials. Following irradiation, a comprehensive analysis of radiation response properties was compiled using X-ray diffraction, nanoindentation, scanning electron microcopy, and transmission electron microscopy. In all cases, the materials remain fully crystalline though atomic collisions induce significant damage and disorder into the layered crystalline lattice. X-ray diffraction and nanoindentation show this damage is manifest in anisotropic swelling and hardening at all conditions and in all materials, with the aluminum based MAX phase exhibiting more pronounced property changes than their silicon counterpart. In all three materials there is little damage dependence on dose (suggesting saturation of radiation damage at levels below 10 displacements per atom) and a high correlation between residual damage and irradiation temperature (with significantly less damage at higher temperatures) suggesting radiation defect annealing. SEM surface analysis showed significant grain boundary cracking and loss of damage tolerance properties in the aluminum based MAX phase irradiated at the low temperature condition. TEM analysis of selected samples suggest that interstitials are mobile while vacancies are immobile and that all three MAX phase are in the so-called "point defect swelling" regime between 400 and 700°C. All results are generally consistent with previous work involving traditional and MAX phase ceramics.

Results show that the aluminum MAX phase is not suitable for application in irradiation environments near 400°C whereas the silicon MAX phase is overall more damage tolerant.

References

[1] 1. Barsoum, M.W., *The Mn+1 AXn Phases and their Properties*, in *Ceramics Science and Technology*. 2010, Wiley-VCH Verlag GmbH & Co. KGaA. p. 299-347.

[2] 2. Barsoum, M.W., *The MN+1AXN phases: A new class of solids: Thermodynamically stable nanolaminates.* Progress in Solid State Chemistry, 2000. **28**(1–4): p. 201-281.

[3] 3. Barsoum, M.W. and M. Radovic, *Elastic and Mechanical Properties of the MAX Phases*, in *Annual Review of Materials Research, Vol 41*, D.R. Clarke and P. Fratzl, Editors. 2011. p. 195-227.

[4] 4. Radovic, M. and M.W. Barsoum, *MAX phases: Bridging the gap between metals and ceramics.* American Ceramics Society Bulletin, 2013. **92**(3): p. 20-27.

[5] 5. Radovic, M., et al., *On the elastic properties and mechanical damping of Ti3SiC2, Ti3GeC2, Ti3Si0.5Al0.5C2 and Ti2AlC in the 300-1573 K temperature range.* Acta Materialia, 2006. **54**(10): p. 2757-2767.

[6] 6. Tallman, D.J., B. Anasori, and M.W. Barsoum, *A critical review of the oxidation of Ti2AlC, Ti3AlC2 and Cr2AlC in Air.* Materials Research Letters, 2013. **1**(3): p. 115-125.

[7] 7. Bugnet, M., et al., *Contribution of core-loss fine structures to the characterization of ion irradiation damages in the nanolaminated ceramic Ti3AlC2.* Acta Materialia, 2013. **61**(19): p. 7348-7363.

[8] 8. Liu, X.M., et al., *Nanoindentation investigation of heavy ion irradiated Ti-3(Si,Al)C-2.* Journal of Nuclear Materials, 2010. **401**(1-3): p. 149-153.

[9] 9. Liu, X.M., et al., *XRD investigation of ion irradiated Ti3Si0.90Al0.10C2.* Nuclear Instruments & Methods in Physics Research Section B-Beam Interactions with Materials and Atoms, 2010. **268**(5): p. 506-512.

[10] 10. Nappe, J.C., et al., *Microstructural changes induced by low energy heavy ion irradiation in titanium silicon carbide.* Journal of the European Ceramic Society, 2011. **31**(8): p. 1503-1511.

[11] 11. Nappe, J.C., et al., *Structural changes induced by heavy ion irradiation in titanium silicon carbide.* Journal of Nuclear Materials, 2011. **409**(1): p. 53-61.

[12] 12. Whittle, K.R., et al., *Radiation tolerance of M(n+1)AX(n) phases, Ti3AlC2 and Ti3SiC2.* Acta Materialia, 2010. **58**(13): p. 4362-4368.

[13] 13. Zhang, L., et al., *Damage tolerance of Ti3SiC2 to high energy iodine irradiation.* Applied Surface Science, 2012. **258**(17): p. 6281-6287.

[14] 14. Marion, L. and I. Monnet, *Saturation of irradiation damage in (Ti,Zr)(3)(Si,Al)C-2 compounds.* Journal of Nuclear Materials, 2013. **433**(1-3): p. 534-537.

[15] 15. Was, G.S. and SpringerLink (Online service), *Fundamentals of Radiation Materials Science Metals and Alloys*. 2007, Springer-Verlag GmbH.,: Berlin Heidelberg.

[16] 16. Zinkle, S.J., *Radiation-Induced Effects on Microstructure*. Comprehensive Nuclear Materials, Vol 1: Basic Aspects of Radiation Effects in Solids/Basic Aspects of Multi-Scale Modeling, ed. R.J.M. Konings. 2012. 65-98.

[17] 17. Tallman, D.J., et al., *Effect of neutron irradiation on select MAX phases.* Acta Materialia, 2015. **85**: p. 132-143.

[18] 18. Barsoum, M.W. and T. ElRaghy, *Synthesis and characterization of a remarkable ceramic: Ti3SiC2.* Journal of the American Ceramic Society, 1996. **79**(7): p. 1953-1956.

[19] 19. Eklund, P., et al., *The Mn+1AXn phases: Materials science and thin-film processing.* Thin Solid Films, 2010. **518**(8): p. 1851-1878.

[20] 20. Stoller, R.E., et al., *On the use of SRIM for computing radiation damage exposure.* Nuclear Instruments & Methods in Physics Research Section B-Beam Interactions with Materials and Atoms, 2013. **310**: p. 75-80.

[21] 21. Toby, B., *CMPR - a powder diffraction toolkit.* Journal of Applied Crystallography, 2005. **38**(6): p. 1040-1041.

[22] 22. *HighScore & HighScore Plus Quick Start Guide*. August 2013; 2nd:[Available from: www.PANalytical.com.

[23] 23. Oliver, W.C. and G.M. Pharr, *An improved technique for determining hardness and elastic modulus using load and displacement sensing indentation experiments.* Journal of Materials Research, 1992. **7**(06): p. 1564-1583.

[24] 24. Nix, W.D. and H. Gao, *Indentation size effects in crystalline materials: A law for strain gradient plasticity.* Journal of the Mechanics and Physics of Solids, 1998. **46**(3): p. 411-425.
[25] 25. Jenkins, L. and A. Kirk, *Characterisation of Radiation Damage by Transmission Electron Microscopy*. 2000: Taylor & Francis.
[26] 26. Jenkins, M.L., *CHARACTERIZATION OF RADIATION-DAMAGE MICROSTRUCTURES BY TEM.* Journal of Nuclear Materials, 1994. **216**: p. 124-156.
[27] 27. DeHoff, R.T., F.N. Rhines, and U.o. Florida, *Quantitative microscopy*. 1968: McGraw-Hill.
[28] 28. Clarke, F.J.P., R.S. Wilks, and D.H. Bowen, *Mechanisms of irradiation-induced growth and cracking in beryllia.* Journal of Nuclear Materials, 1964. **14**: p. 205-207.
[29] 29. El-Raghy, T., et al., *Damage Mechanisms around Hardness Indentations in Ti3SiC2.* Journal of the American Ceramic Society, 1997. **80**(2): p. 513-516.
[30] 30. Iseki, T., et al., *HARDENING BY POINT-DEFECTS IN NEUTRON-IRRADIATED ALN AND SIC.* Journal of Nuclear Science and Technology, 1993. **30**(1): p. 68-77.
[31] 31. Snead, L.L., et al., *Amorphization of SiC under ion and neutron irradiation.* Nuclear Instruments & Methods in Physics Research Section B-Beam Interactions with Materials and Atoms, 1998. **141**(1-4): p. 123-132.
[32] 32. Suematsu, H., et al., *POINT-DEFECT HARDENING IN MGO.3AL2O3.* Journal of the American Ceramic Society, 1992. **75**(7): p. 1742-1747.
[33] 33. Yang, Y., et al., *Microstructure and mechanical properties of proton irradiated zirconium carbide.* Journal of Nuclear Materials, 2008. **378**(3): p. 341-348.
[34] 34. Snead, L.L. and S.J. Zinkle, *Use of beryllium and beryllium oxide in space reactors*, in *Space Technology and Applications International Forum-Staif 2005*, M.S. ElGenk, Editor. 2005. p. 768-775.
[35] 35. Zinkle, S.J. and B.N. Singh, *Microstructure of neutron-irradiated iron before and after tensile deformation.* Journal of Nuclear Materials, 2006. **351**(1-3): p. 269-284.